63-3-4

hp associates • 2900 park boulevard • palo alto, california • DA 1-8510

Interim Engineering Report No. 2

ADVANCED FUNCTIONAL ELECTRONIC BLOCK DEVELOPMENT

1 December 1962 to 28 February 1963

Air Force Contract No. AF33(657)-9772
BPSN: 3-6799 760E 415906

The applied research and advanced development reported in this document has been made possible through the sponsorship extended by the Electronic Technology Laboratory of the Aeronautical Systems Division under Contract No. AF33 (657)-9772, BPSN: 3-6799 760E 415906. It is published for technical information only, and does not necessarily represent recommendations or conclusions of the sponsoring agency.

ABSTRACT

The report is grouped into six chapters.

In Chapter I, the continued exploration of optical, structural and ferroelectric properties of SbSI is described. A comparison of reported values of the shift of optical absorption edge with electric field in several materials brought out that this effect is at least an order of magnitude larger in SbSI than in any other material.

In Chapter II, the continued effort on photosensors is described. Two distinct families of npn planar silicon phototransistors have been developed. One with gain β of 80-120 and the other of 600-800. The photoelectric collection efficiency is highly uniform over the exposed base and is approximately 50%. The speed of response of the phototransistors is a function of light intensity, collector capacitance and gain, and emitter capacitance.

Chapter III deals with experimentation on injection electroluminescence and is further subdivided in sections on zinc diffused GaAs pn junctions, n on p GaAs alloyed junctions, GaAs-CdS pn heterojunctions and BP luminescence.

Two studies have been carried out on zinc diffused GaAs junctions. The first deals with effect of Cu on electroluminescence in GaAs. The second concerns fine structure in "Edge Electroluminescence" spectra.

The work on electroluminesence from diodes made by alloying AgTe dots onto p-type GaAs continued. The most efficient diodes were made on GaAs with hole concentrations about $2x10^{17}$ acceptors/cm^3.

Heterojunctions of n-type CdS on p-type GaAs have been fabricated. The energy discontinuity of the conduction band edges at the junction has been determined to be 0.2 eV. The saturation current has been found to be far in excess of that expected.

The effects of doping on the far infrared absorption in GaAs have been investigated. It was found that above defect concentrations of $10^{17}/cm^3$ the restrahlen bands were wiped out.

The electroluminescent spectrum of rhombohedral boron phosphide has been obtained.

In Chapter IV on optoelectronic pairs, preliminary experiments leading to the development of an optimum optical match between the el diodes and photosensors are described.

In Chapter V various instrumentation built or installed during the last period in support of the program is described. These include a power supply for the thermoelectric cooler, the installation of a new double beam grating spectrophotometer, construction and installation of an optical cryostat of novel design and the development of a new synchronous sampling technique for the spectrophotometer.

In Chapter VI all of the materials synthesis and crystal growth effort is described. It includes gallium arsenide epitaxial growth by vapor transport, boron phosphide growth from solution, evaporation of CdS thin films onto GaAs substrates and the synthesis of high refractive index glasses.

TABLE OF CONTENTS

CHAPTER I

EXPLORATION OF SOLID STATE EFFECTS

Work has continued during the past quarter on the study of the optical, structural, and ferroelectric properties of SbSI. Results of this work are summarized below.

I.1. Optical Properties

Several SbSI crystals were measured for optical absorption as a function of wavelength, and a representative curve is shown in Figure I-1. For comparison, similar measurements by Kern[1] are shown, and also our measurements on SbI_3 are indicated. The smearing out of the absorption edge in our crystals suggested the possibility of structural imperfections, deviations from stoichiometry, and possibly admixtures of other components. The absorption measurements on SbI_3 indicate that the smearing effect is not due to admixtures of this component, since the edge is fairly abrupt in comparison and extends to wavelengths even shorter than either of the SbSI plots. Attempts were made to determine the effects of strain and temperature variation on the position of the absorption edge in SbSI. Because of the small size of crystals available at the time, it was not possible to obtain satisfactory results.

A comparison was made between the reported values of the shift of optical absorption edge with electric field in several materials. These data are summarized in Table I-1. The point of interest is that the effect in SbSI[1] is at least

TABLE I-1

Material	Electric Field (volt/cm)	Change in Absorption Edge (eV)	References
SbSI	5×10^3	2.6×10^{-2} (+)	R. Kern; J. Phys. Chem. Solids, 23, 249 (1962)
GaAs	5×10^3	2×10^{-4} (-)	T. S. Moss; J. Appl. Phys. 32, 2136 (1961)
CdS	10^6	3.3×10^{-2} (-)	R. Williams; Phys. Rev. 117, 1487 (1960)
PbI_2	9×10^5	1.1×10^{-2} (-)	R. Williams; Phys. Rev. 126, 442 (1962)
HgI_2	Similar to PbI_2		R. Williams; Phys. Rev. 126, 442 (1962)
Si	$5 \times 5 \times 10^4$	1.9×10^{-2} (-)	L. V. Keldysh; Proc. Int. Conf. Semicond. Phys., Prague 1960, 824, Academic Press 1961

an order of magnitude larger than in any of the other materials, and that it is in the opposite direction (toward higher energy) to what would be expected from theoretical considerations.[2] This striking effect, which is visible to the eye, was qualitatively demonstrated on our SbSI crystals. A change of approximately 70Å in the absorption edge was induced by the application of an electric field of 5 kv/cm. Considerations are being given to the possibility of using this field-induced shift of optical absorption for modulating nearly monochromatic electroluminescence. The effect is especially interesting in SbSI and related V-VI-VII compounds, because the position of the absorption edge can be varied by changes in composition and stoichiometry.[3]

I.2. Structural Properties

Several Laue back-reflection x-ray pictures were taken of SbSI crystals in the vicinity of the Curie temperature, to determine the change in structure as the material goes through the paraelectric → ferroelectric transition. Both the temperature and the applied electric field were varied. A doubling was observed in several of the spots on the x-ray picture with the application of an electric field below the Curie temperature. It was not possible to make a quantitative interpretation of the observed effect because the spots were not well defined. This measurement will be repeated when better crystals are synthesized in the future.

I.3. Ferroelectric Properties

Measurements were made of the spontaneous polarization and coercive field in SbSI, as a function of temperature. These data are shown in Figure I-2 for several crystals. On the same graph are plotted similar data from Fatuzzo, et al.[3] The values of the spontaneous polarization reported by Fatuzzo, et al are twice those measured in our laboratory, whereas, the coercive fields are about six times less than our measured values. In the case of other ferroelectric materials, it has been observed that, as better crystals are grown, higher values of P_s and smaller values of E_c are reported.

In Figure I-3 is a photograph of a representative hysteresis loop of an SbSI crystal grown in our laboratory.

An experimental transpolarizer[4] employing SbSI exhibited charge storage of the order of a few seconds. The relaxation of a stored setting is probably due in part to the photoconductivity.

An investigation was made of the effects of shunt and series photoconductivity on the shape of the ferroelectric hysteresis loop. These were compared with the effect of direct illumination on the ferroelectric hysteresis loop. The distortion of the loop could be accounted for, to first order, by the shunt conductivity due to illumination. It was also concluded that the photoferroelectric effect, if present, is probably less than 5% of the above first order effect.

REFERENCES (Chapter I)

1. R. Kern; J. Phys. Chem. Solids, 23, 249 (1962).

2. W. Franz; Z. Naturforsch, 13a, 484 (1958).

3. E. Fatuzzo, et al; Phys. Rev. 127, 2036 (1962).

4. C. F. Pulvari; Proc. IRE, 47, 6, 1117 (1959).

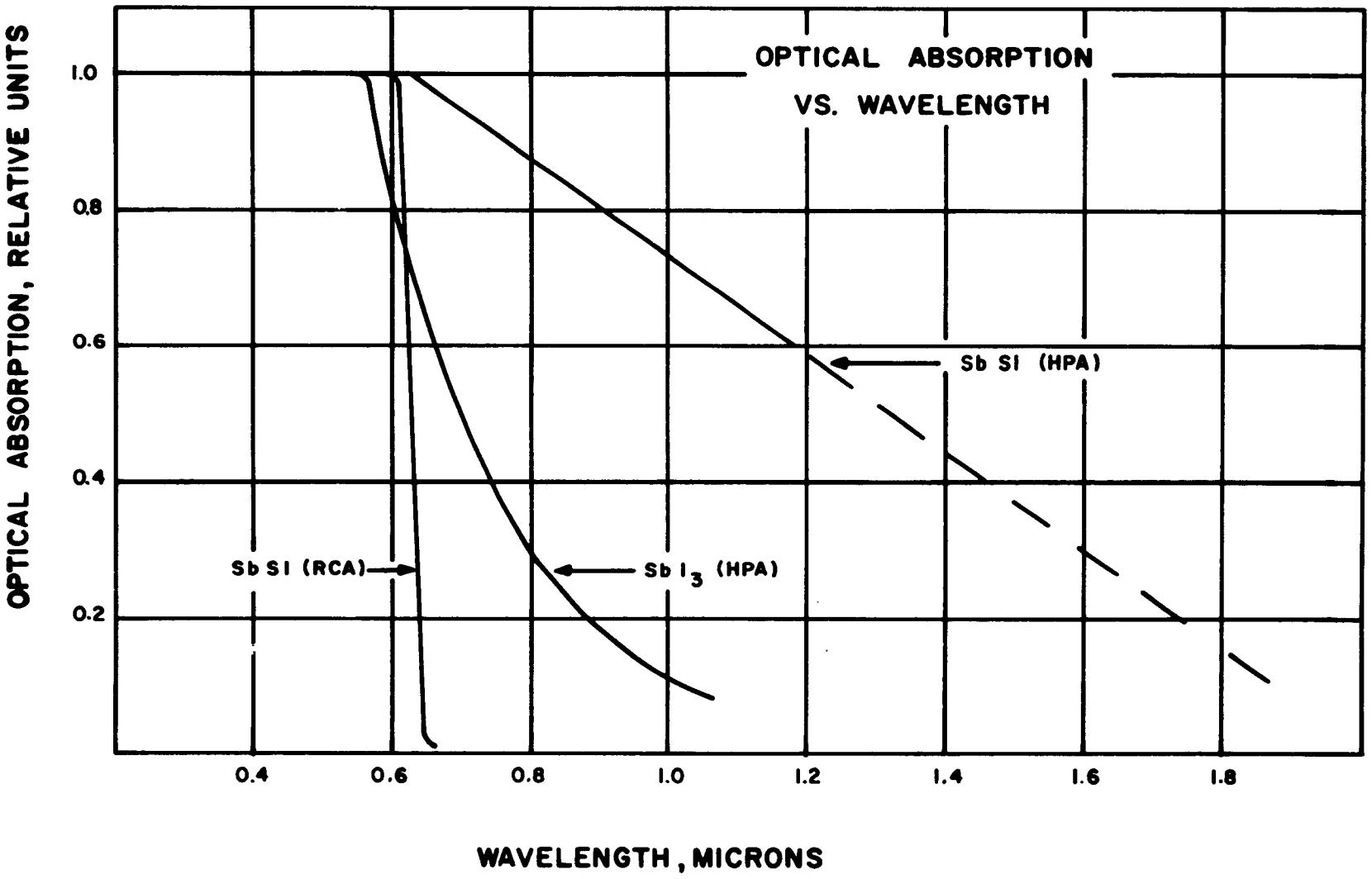

I-1

Spectral Dependence of Optical Absorption in Crystals of SbSI and SbI_3.

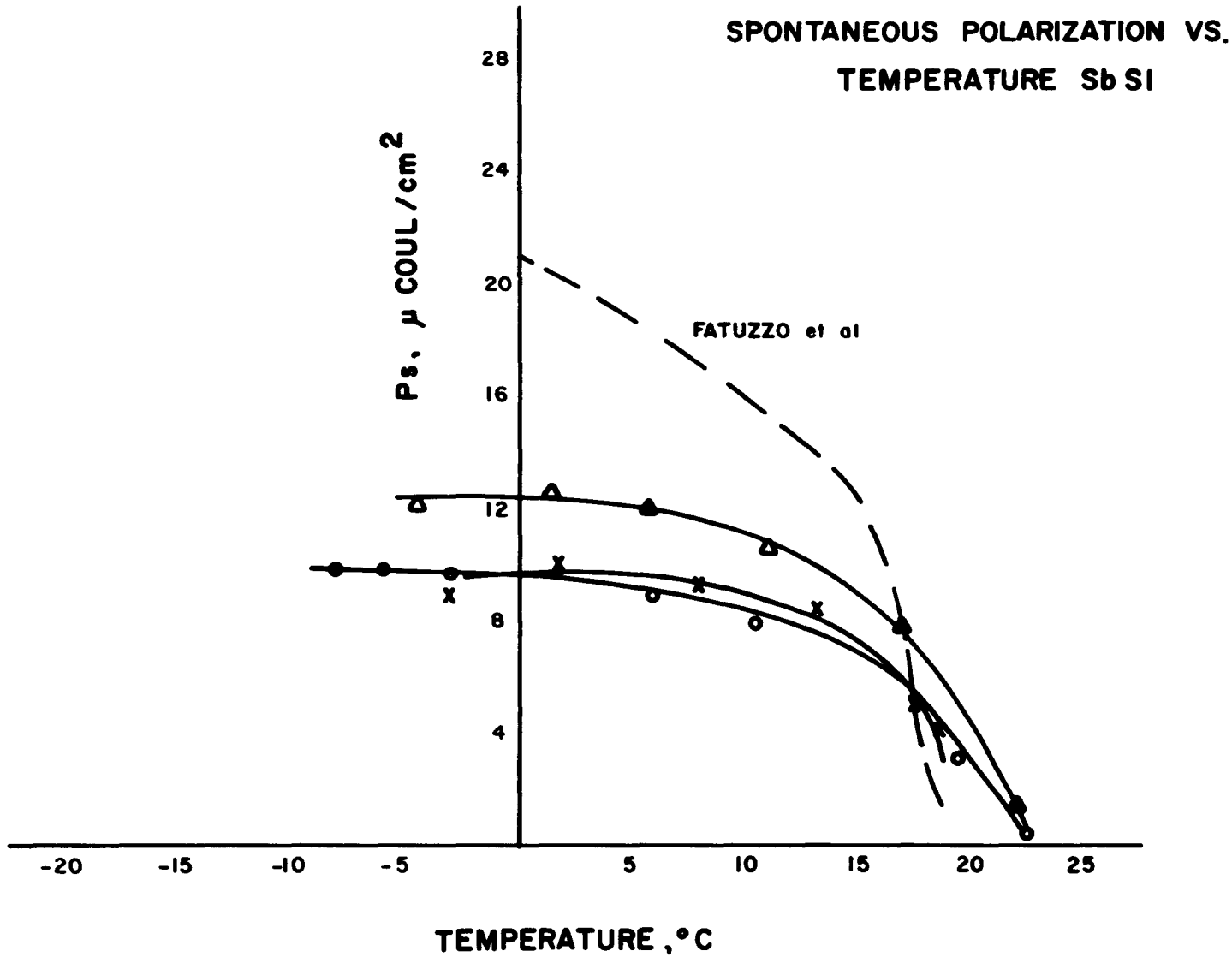

Fig. I-2. Spontaneous Polarization in SbSI as a Function of Dependence.

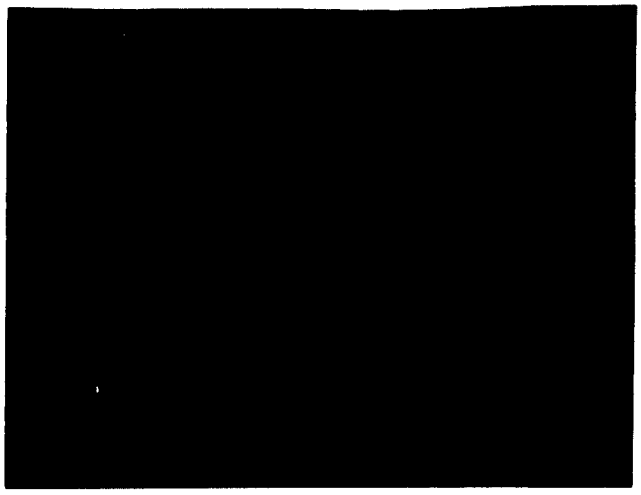

Fig. I-3. Hysteresis Plot of the Representative SbSI Crystal.

CHAPTER II

PHOTOSENSORS

II.1. npn Silicon Phototransistors

Considerable progress has been made in the development of special phototransistors suitable for paring with gallium arsenide el diodes. As described in the First Interim Engineering Report, the main effort continued on the npn planar silicon structure in an attempt to obtain both high sensitivity and high gain.

II.1.1. Structure and Electrical Characteristics

Transistors of the following geometry were used: emitter diameter 0.005", collector diameter 0.040", and base layer width of 0.8 to 1.0 micron. Two distinct families of phototransistors have been developed; one of intermediate gain of 80-120, and the other of high gain of 600-800.

β:	common emitter current gain @ I_C = 3 ma	600-800
C_{EBO}		25 pf
C_{CBO}		120 pf
V_{BCE}		8-15 volts

Figure II-1 shows typical common emitter electrical characteristics of one phototransistor with a gain β of about 600.

Photo-sensitivity and photo-response measurements were also carried out on these transistors. These are summarized in the following two sections.

II.1.2. Phototransistor Sensitivity

A uniform diffused light field was produced using a 300 watt 35 mm slide projector (infrared filter removed) with diffusers and a sharp bandpass filter (Figure II-2). The filter had a ± 3% transmission passband centered at about 910 μu, hence, closely approximated GaAs el diode emission. Intensity of this light source was measured in terms of the short circuit current that was produced in a silicon solar cell of known efficiency.

This light flux was then applied to the phototransistor and the resulting current measured. Since the radiation flux density and the sensitive surface area were known, the quantum gain of the phototransistor could be determined. Furthermore, from a knowledge of the phototransistor common emitter gain β as determined by electrical measurements, it was possible to find the collection efficiency of the phototransistor. For phototransistors with the geometry described above, collection efficiencies of about 50% were measured.

To test the uniformity of the large area photosensitive base regions, we have investigated the topography of the photo-sensitive area on a phototransistor. A spot of white light having a diameter of about 0.0035" was scanned across the exposed photosensitive p-region and the electrical response of the device (emitter to collector) was recorded as a function of position. In Figure II-3, the iso-response lines measured are shown, indicating good uniformity of photosensitivity over the base region area of the phototransistor.

II.1.3. Phototransistor Speed of Response

The instrumentation used for evaluating the speed of response of the phototransistor is shown in Figure II-4. It consists of a gallium arsenide el diode with square wave excitation, and an optical coupling system. Light pulses were applied to the sensitive area of the phototransistor and its transient response observed.

Figure II-5 shows typical photo-response traces for a phototransistor with a common emitter current gain β of about 100. Characteristic features are: (1) signal delay time corresponding to the time of charging the emitter by the light generated carriers; (2) rise time, corresponding to the time of discharging the collector (to a lower voltage) by the generated carriers (the effective collector capacitance is β times its transition capacitance). For these transistors, the minority carriers transit times were less than 0.1 μsec and, hence, did not contribute to the responses observed.

To reduce the total response times, lower capacitance structures will be made by reducing junction areas and using higher resistivity epitaxial silicon.

II.2. Photoconductors

In addition to silicon phototransistors, which represent photosensors of high speed and moderate gain, it may be advantageous to consider photoconductors of moderate speed and high gain. Unfortunately, the .8 to 1.3 micron range of the spectrum has not been intensively studied in the past

from the point of view of providing optimum photoconductive parameters useful in optoelectronic networks incorporating GaAs el diodes operated at room temperature.

We have begun a survey of the dependence of the various significant parameters on photoconductor materials. So far, we have investigated CdTe, semi-insulating GaAs and PbS photoconductors.

The CdTe sintered photoconductors lack the required spectral response. They show insufficient sensitivity beyond .83μ. Semi-insulating GaAs has a reasonable spectral response, but appears to have marginal sensitivity. So far, the most encouraging results have been obtained with lead sulfide. Using a type "O" Kodak Ektron lead sulfide photoconductor with an electrode spacing of 20 microns and gap length of 2000 microns, a comparative test was made with a silicon phototransistor exposed to the same el diode under identical geometry, current pulsing and applied voltage conditions. The results indicated the response of the PbS cell to be about 20% higher than for a Si phototransistor with a common emitter gain $\beta = 80$. Its speed of response, however, was significantly lower. The rise time observed was 200 μs and the decay time 300 μs. Furthermore, at room temperature, the dark current of the PbS cell was excessively high, being about twice the photocurrent. This can, in part, be corrected by improved electrode geometry.

Fig. II-1. High Gain Phototransistor-Collector Characteristics.
Vertical Scale: Collector Current, 1 ma/cm
Horizontal Scale: Collector Voltage, 1v/cm
Base Current: 5μa/step

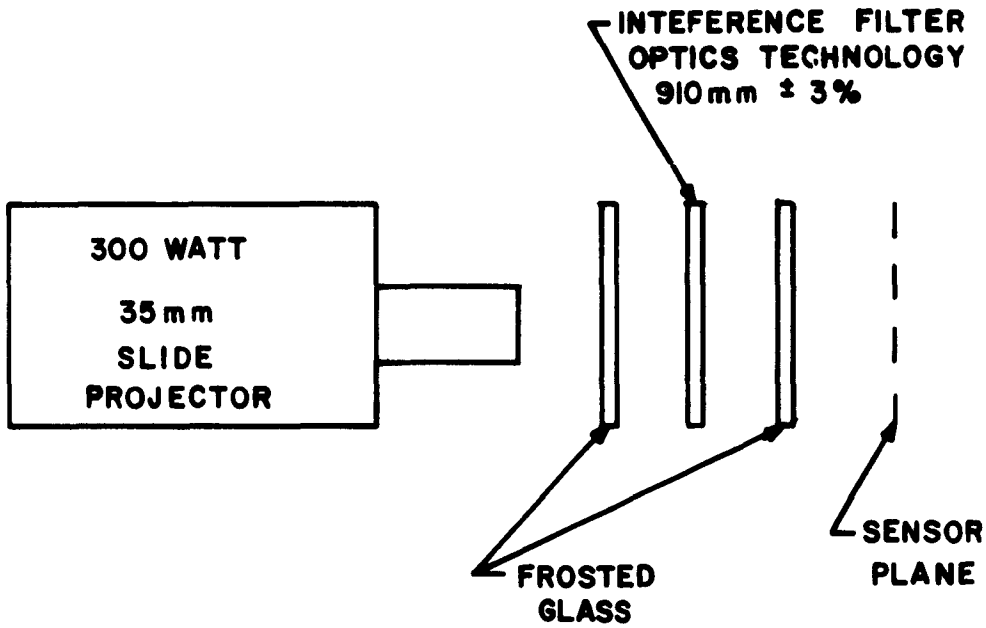

Figure II-2. Photodetector Sensitivity Evaluation

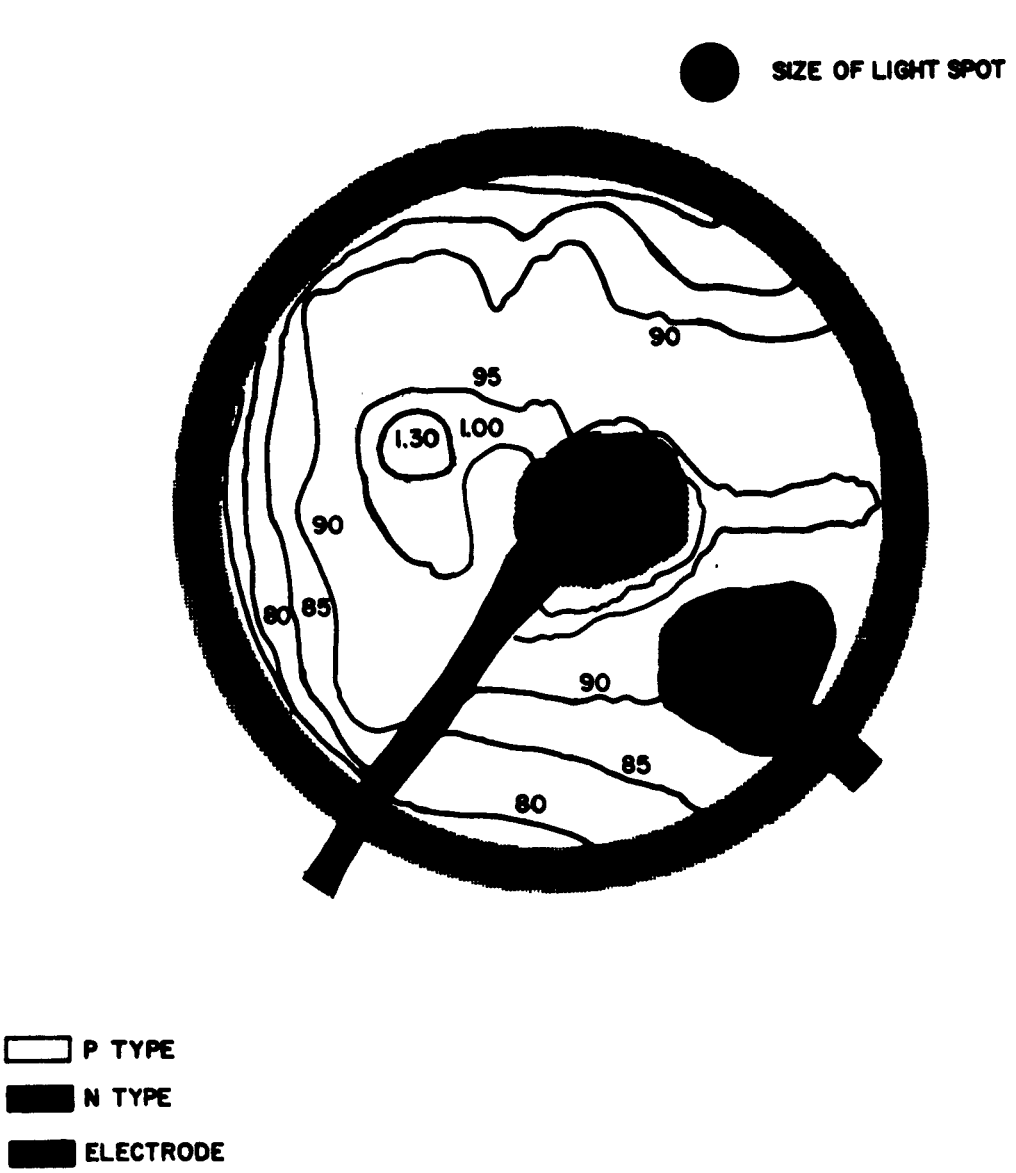

Figure II-3. Photoelectric Iso-Response Lines of an npn Phototransistor.

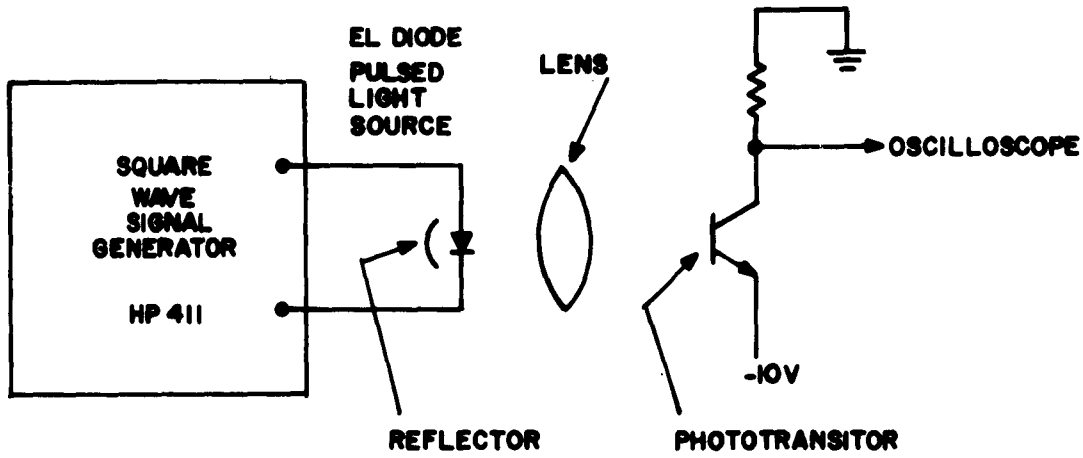

Figure II-4. Experimental Setup for the Measurement of the Transient Response of Phototransistors.

Figure II-5. Phototransistor Response for Stepped Intensity Light Pulses.
Vertical Scale: Collector Current, 200 μa/cm
Horizontal Scale: Time, 2 μsec/cm

Note: The increased delay and rise time for low light intensity is due to a correspondingly increased charging time for the emitter base capacitance.

CHAPTER III

INJECTION ELECTROLUMINESCENCE

Studies of injection electroluminescence were carried out on zinc diffused GaAs pn junctions, AgTe alloy n on p GaAs junctions, CdS-GaAs heterojunctions, and BP diodes. The work on diffused junctions and heterojunctions concentrated heavily on the elucidation of the mechanisms of injection electroluminescence. The investigation of alloy GaAs junctions was directed toward finding the optimum carrider concentration. In boron phosphide, differences between light emission from cubic and rhombohedral single crystals were investigated.

III.1. Zinc Diffused GaAs Junctions

III.1.1. The Effect of Cu on Electroluminescence in GaAs

III.1.1.1. Introduction

In the optical emission spectra of forward biased GaAs diodes, several investigators have reported two energy peaks:[1,2,3] a near edge emission peak at about 1.37 eV and a broad energy peak centered near 1.0 eV at 300°K. Up to the present, apparently little attention has been given to the effect on the luminescence of such defects as copper contaminants and stoichiometry defects resulting from heat treatments. The effect of Cu impurities on luminescence in GaAs is particularly interesting, since it is an acceptor impurity which diffuses readily at relatively low temperatures.[4] During heat

treatments, Cu contamination can occur from such sources as quartz ampoules[5] and the C.P. grade reagents usually used to clean and etch GaAs.[6]

At temperatures near 700°C, the solubility of Cu in GaAs is about 10^{17}/cc,[4,7] and has been shown to level off to a value slightly above 10^{16} at temperatures below 600°C.[7] With quenched-in Cu concentrations of these orders of magnitude, compensation of carriers in the 10^{17} donors/cc material used for the diode base can make the resistivity approach the intrinsic value. This compensation of carriers on the n side of the pn junction will influence the injection of minority carriers, their recombination and, therefore, possibly the radiative transitions. Also, crystal annealing after Cu diffusion has been shown to introduce very large concentration of lattice defects.[9]

In this investigation, the source of the 1.0 eV emission peak is identified and the effect of Cu contamination and heat treatment on the efficiency of luminescence is evaluated.

III.1.1.2. Experimental Procedure and Techniques

In this experiment, nine speciments, divided equally into three groups, were subjected to a variety of diffusions and heat treatments. One group was purposely doped with copper while, for the sake of control, one other group was given an identical heat treatment without Cu and the third was untreated. Following this, a zinc-diffused pn junction was

formed in all specimens. One specimen in each group was then gettered in liquid Ga, another identically heat-treated and the third given no further treatment.

Except for batch Dy-35, spectrographically pure quartz ampoules were used in all heat treatments to protect against possible Cu contamination from the standard grade quartz normally used. Batch Dy-35 was Zn diffused in the lower grade quartz.

All specimens, except those from batch Dy-35, were taken from one single crystalline wafer of Sn doped GaAs having 1.5×10^{17} donors/cc. (Dy-35 was taken from another slice of the same ingot.)

An evaporated layer of Cu was diffused into specimens comprising batches Dy-51, 52 and 53 (see Table III-1) in an evacuated ampoule at 600°C for 90 hours, after which the ampoule was quenched in air. Upon removal of residual Cu from the surfaces, the specimens were sealed in an evacuated 10 cc ampoule with 4 mg Zn, diffused at 800°C for 10 minutes and ther cooled in air.

Specimens comprising batches Dy-54, 55 and 56 (see Table III-1) were heat treated, without Cu, under identical conditions prescribed for the Cu diffusion above and then Zn diffused. Speciments from batches Dy-57, 58 and 59 were not treated prior to the Zn diffusion.

Since Ga gettering of Cu from GaAs has been proven effective,[7] batches Dy-52, 55 and 58 (see Table III-1) were

gettered by floatation on liquid Ga at 500°C for 90 hours in an evacuated ampoule. To insure Ga wetting, a layer of Ga was first evaporated on the <111> face of the GaAs.

Specimens from batches Dy-53, 56 and 59 (See Table III-1) were heat treated similarly to the gettering conditions above. The remaining three batches were left untreated after the Zn diffusion.

With the completion of the aforementioned treatments, the pn junction was lapped from the <111> sides of the chips. Aluminum alloyed at 600°C formed the p-side contact. AuSn alloyed near 400°C provided the base or n-contact. Mesa diodes were fabricated and mounted in TO-5 headers by the standard techniques already described in the First Interim Engineering Report.

The optical properties of the diodes were characterized by measuring the emission spectra with a Beckman spectrophotometer, type DK-1A, using a PbS detector, and by measuring the relative light output with an RCA Multiplier Phototube, type 7102, having an S-1 response. Copper impurity concentrations were determined by emission spectrographic analysis.

III.1.1.3. Results

III.1.1.3.1. Luminescence Spectra

In Figure III-1, emission spectra are recorded for two diodes: Dy-51-4, typifying specimens with a broad peak centered near 1.0 eV at 300°K in addition to the main energy peak at 1.37 eV; and Dy-54-1, typifying specimens with only

the 1.37 eV peak. Table III-1 lists in Section b the average ratio of integrated energy in the 1.0 eV peak to that in the higher peak for each specimen. These data show that specimens in which Cu was purposely introduced emit from 20-30% of the combined energy at 1.0 eV, while the other six specimens show less than 1% in the lower peak. Dy-35 gave a 1.0 eV radiation contribution of about 10%.

III.1.1.3.2. Copper Impurity Concentrations

The concentrations of Cu impurities after treatments, as determined by emission spectrographic analysis,[10] are given in Table III-1, Section c. Although gettering by liquid Ga was effective in decreasing the Cu concentration from about 20 ppm in Dy-51 and Dy-53 to 2 ppm in Dy-52, the Cu doping was still sufficient to create 1 eV emission.

The detectibility limit of Cu in GaAs was 1 ppm or about 4×10^{16}/cc. This concentration is very nearly that expected in saturated samples quenched from 600°C.[4,7] Since 1.0 eV emission was detected in Dy-35, having less than 1 ppm, and approached the maximum in Dy-52 with only 2 ppm of Cu, the excess or precipitated copper in Dy-51 and 53 seems not to enhance the lower energy peak.

III.1.1.3.3. Luminescence Efficiency

The relative light outputs of a few diodes from each specimen were measured with a type S-1 response photomultiplier (not sensitive at 1.0 eV) and tabulated in Table

III-1, Section c. The average for each specimen is indicated. In the next line, the averages are again shown with the 1.0 eV energy added, and a group average is also indicated.

Comparison of the relative efficiencies shows that these particular treatments do not grossly affect the 1.37 eV emission. The deviation of batch averages is no more than a factor of three, and in some cases no greater than the scatter within a batch. However, an evaluation of the statistical averages does sh. that the addition of the 1.0 eV energy peak to the average 1.37 eV peak very closely equalizes the averages between group I and group II.

III.1.1.4. Discussion

The most important results of this investigation has been the attribution of the broad emission peak near 1 eV in GaAs to copper impurities. The mechanism for this radiative process remains undefined. Comparison of the Cu ionization energy, 0.14 eV, with the 1.41 eV bandgap of GaAs at 300°K does not suggest 1 eV energy to be emitted from recombination of carriers undergoing direct transition between the conduction band edge and this Cu acceptor level.

The data does indicate a transfer of the energy emitted in the near edge emission peak into the 1 eV peak. Evidence also supports the belief that the efficiency of the lower energy emission is influenced directly only by soluble Cu and that the excess or precipitated Cu is relatively inactive.

This point might be clarified by an experiment in which higher concentrations of Cu were quenched into the GaAs.

Although little is known of the exact nature of el mechanisms in GaAs, qualitative models are worthwhile in interpreting this type of data. Consider, then, a model in which minority carriers are injected across a forward biased pn junction and recombine, some radiatively and some not. By predicating this model on the evidence reported by Nathan and Burns,[11] and also indicated by our alloy junction studies on p-type GaAs (See First Interim Engineering Report), the near edge emission is assumed to originate in the p-region only. The non-radiative mechanisms are assumed to be active on both sides of the junction.

By introducing Cu impurities, the donors are compensated and the acceptor density is slightly enhanced. Since, in this model, the efficiency, η, of edge emission is proportional to the injection efficiency, γ, where $\gamma = I_e/I_e+I_p$, and since the compensation decreases γ, the presence of Cu decreases η. On the basis of spectrographic analysis and available solubility data, an estimate of 1 ppm or about 4.5×10^{15} Cu compensators were active. This is a sufficient number to compensate 25% of the 1.5×10^{17} donors present in the diode base region. This should, therefore, cause a 25% decrease in electron injection efficiency and, consequently, a 25% decrease in 1.37 eV photon efficiency. Referring then to Table III-1, Section d, and comparing group I with group II, the average efficiency of group I without the addition of 1 eV energy is

TABLE III-1

	Group I			Group II			Group III			
	Dy-51	Dy-52	Dy-53	Dy-54	Dy-55	Dy-56	Dy-57	Dy-58	Dy-59	Dy-35
a. Treatments*	Cu Zn --	Cu Zn Get	Cu Zn H.T.	H.T. Zn --	H.T. Zn Get	H.T. Zn H.T.	-- Zn --	-- Zn Get	-- Zn H.T.	-- Zn --
b. Ratio:1 eV:1.37 eV Intergrated energies	.29	.30	.17	.01	.01	.01	.01	.01	.01	.10
c. Cu Concentration PPM	20-21	2	19-20	1	1	1	1	1	1	1
d. Relative Luminescent Efficiencies	.12 .28 .44 .54 .40	.54 .70 .44 .75	.42 .42 .48 .38 .52 .34	.65 .50 .55 .50 .44 .65	.80 .85 .90 .85 .65 .55 .60	.43 .75 .65 .85 .70 .56	.42 .46 .36 .43 .34 .26 .34	.26 .30 .27 .24 .25	.60 .55 .50 .75 .50	
Specimen Avg.	.36	.61	.43	.55	.74	.66	.37	.26	.58	
Group Avg. w/o 1 eV added		.47			.65			.40		
Specimen Avg. with 1 eV added	.50	.87	.51	.55	.74	.66	.37	.26	.58	
Group Avg.		.63			.65			.40		

*Cu: Copper Diffusion H.T.: Heat Treatment --: No Treatment
Zn: Zinc Diffusion Get: Ga Getter

28% less than the average of group II. This agreement seems to support this model.

The presence of Cu introduces a second radiation mechanism, the efficiency of which is also dependent on the soluble Cu concentration, and which may be active either in the n or p region. Nathan and Burns[12] have reported the 1 eV emission to originate in n-type GaAs. The experimental data presented here are consistent with their observation.

The 1 eV emission observed from our standard el sources results from Cu contamination occurring during the zinc diffusion in lower purity quartz.

III.1.2. Structure in "Edge Electroluminescence" Spectra

Our study of the emission spectrum of GaAs diodes has been continued, using the synchronous sampling technique described in Section V.4. The results of a number of runs made at room temperature with one of our el diodes are shown in Figures III-2, III-3 and III-4. The diode was pulsed at the rate of 13 pulses/sec, with a pulse width of 21 μsec, and at current levels varying from 25 to 310 ma. The photomultiplier output pulse (Figure III-2, as seen on the sampling scope) was sampled at its peak, 20 μsec after its inception, for a 21 μsec period, i.e., the duration of the diode current pulse. The slow rise is due to the large resistor used to obtain the output voltage. It is clear from Figure III-3 that two peaks are present, one at 1.37 eV and the other at 1.41 eV and that their positions do not change throughout the range of currents

used. Figure III-4 indicates the ratio of the heights of the two peaks as a function of forward current through the el diode. It is seen that the height of each peak increases approximately linearly with increasing current and that there appears to be a common cutoff current for both emissions below which there is no emission. Extrapolating our data to zero light emission, this current is 18 ma, for a 21 μsec duration pulse.

The half-widths of the two peaks are 0.035 eV for the more intense 1.37 eV peak and 0.045 eV for the 1.41 eV satellite peak. These widths were obtained by reflecting the 1.41 eV peak through its center line and by subtracting its contribution from the 1.37 eV peak width, to get the estimated width of the 1.37 eV peak (See Figure III-5). Since the peaks are separated by only 0.040 eV, which is slightly less than the half-width of the broader peak, and since the 1.41 eV peak is only about one-fourth the height of the 1.37 eV peak, they are just barely resolvable. It seems likely that the structuring of the emission into two peaks could not be observed earlier without the high sensitivity of synchronous sampling (Section V.4.) and the very slow scan speed employed during experiments. It should be recalled that Figure 33 of our First Interim Engineering Report also showed structure containing a secondary peak at 0.880μ in the el emission from alloyed GaAs junctions.

An explanation of the structure in the room temperature spectrum of "edge electroluminescence" may contribute

to our understanding of the optical properties of GaAs. It should be noted that the 1.41 eV emission coincides with the position of the extrapolated absorption edge in pure GaAs.[13] Thus, one may surmise that this peak could result from direct recombinations of free electrons and free holes, while the 1.37 eV should be assignable to recombinations via localized defect states. However, the constant ratio of these peaks, their common current threshold and the significantly greater width of the 1.41 eV peak, detract somewhat from this possibility.

It appears reasonable to consider the assignment of the 1.41 peak to phonon assisted transitions of the 1.37 eV peak. Thus, a phonon of approximately 0.04 eV energy is captured and contributes its energy to the emitted photon. It is interesting to note that Hall and coworkers[20] have observed a 0.036 eV LO phonon assisting tunneling across GaAs tunnel diode pn junction. Also, the optical phonon spectrum of GaAs, as discussed in Section 4 of this chapter, appears consistent with such an assumption. Further experiments are underway to distinguish between the various possible mechanisms.

III.2. GaAs Alloy Junction Experiments

As reported in the First Interim Engineering Report, light emitting diodes have been made by alloying small AgTe (1%) spheres on p-type GaAs. Since the near edge emission is believed to originate in the p-regions, and since light sources of comparable efficiency to the standard zinc diffused diodes

have been made, this structure is of particular interest.

At present, very little is known about this junction, however. A series of tests have been run to determine the dependence of the el efficiency on base material doping type and concentrations. In Figure III-6 the relative emitted radiation efficiencies are plotted as a function of the concentrations in p-type GaAs doped with Cd, Zn and Mn acceptors. The luminescence data on Cd and Zn doped samples both indicate the dependence shown by the dashed curve.

From these data then, we deduce that the most efficient AgTe (1%) alloyed junctions occur at about $2x10^{17}$ carrier/cc for Zn or Cd doped GaAs. On the low concentration side of the maximum, the efficiency increases by one order of magnitude with one order of magnitude increase in carrier concentration. These data substantiate the linear dependence of efficiency on acceptor concentration recently proposed by W. P. Dumke.[14]

The sharp decrease in efficiency at large concentrations may, in part, be attributed to internal absorption, since the absorption coefficient increases by about an order of magnitude in the range between 10^{17} and 10^{19} carriers/cc.[15] The major cause of decreased efficiency at concentrations above $4x10^{17}$ may, however, be due to decreasing efficiency of electron injection into the p-region.

III.3. Cadmium Sulphide-Gallium Arsenide Heterojunction Diodes

A variety of heterojunctions were described briefly in our First Interim Engineering Report. In this report period we have concentrated on one specific type of heterojunction, viz, a diode consisting of an evaporated n-type CdS heterojunction to a p-type GaAs crystal. It is, therefore, appropriate to describe in detail the nature of this heterojunction and the characteristics that it is expected to exhibit.

The electron energy diagram of a CdS-GaAs junction of this type is shown in Figure III-7. The n-type CdS is shown much more heavily doped than the p-type GaAs, which is likely to be the case for evaporated CdS, so that most of the built-in voltage is taken up on the GaAs side of the junction. The energy discontinuity of the conduction band edges at the boundary, Δ, is given by

$$\Delta = \chi_{CdS} - \chi_{GaAs}$$

where χ is the electron affinity of each material in contact with the other. These values may not necessarily be the same as those measured with each surface exposed to vacuum or to a third material, so Δ must be determined experimentally. In addition, the electron affinity is likely to be different for different crystal faces. As an indication, however, data from this laboratory show that $\chi_{CdS} = 4.0$ eV and $\chi_{GaAs} = 3.8$ eV for junctions to gold. From this, one might expect $\Delta \approx 0.2$ eV.

The principal advantage of this structure over a diffused or alloyed diode structure is that this heterojunction

will provide essentially 100% injection efficiency of electrons into even degenerate p-type GaAs. The injected minority carrier currents, J_e and J_p, are determined in each case by the diffusion of minority carriers away from the junction, as is the case with homojunctions. They are then given by

$$J_e = q \frac{N_c N_v}{p_p} \frac{D_n}{\tau_n} e^{-\frac{qE_g}{kT}} [e^{\frac{qV}{kT}} - 1] \quad (1)$$

and

$$J_p = q \frac{N_c' N_v'}{n_n'} \frac{D_p'}{\tau_p'} e^{-\frac{qE_g'}{kT}} [e^{\frac{qV}{kT}} - 1] \quad (2)$$

where q is the electronic charge, N_c and N_v are the effective densities of states in the conduction and valence bands, respectively, D_n and τ_n are the diffusion coefficients and lifetimes, respectively, of the minority carriers, p_p is the majority carrier density and E_g is the bandgap of the material. The unprimed quantities refer to the GaAs and the primed quantities to the CdS. The ratio J_e/J_p is proportional to $\exp[q/kT(E_g'-E_g)]$ $= 2.5 \times 10^{18}$ at 300°K, taking $E_g' = 2.5$ eV and $E_g = 1.4$ eV. Even if $p_p = 10^{20}/cm^3$ in the GaAs and $n_n' = 10^{15}/cm^3$ in the CdS, the electron injection will completely dominate. This feature is particularly useful in determining experimentally the dependence of injection luminescence on acceptor density.

A second advantage of this heterojunction is that the CdS can be made quite transparent at 0.91μ wavelength and simultaneously provide a sheet resistance of 1Ω, allowing uniform spreading of current from the contacts. (See Chapter VI

of this report.) In both alloyed and diffused junctions, half of the light must pass through a relatively highly absorbing GaAs layer. Finally, the heterojunction is an excellent aid to materials process evaluation since the injecting contact can be made at a sufficiently low temperature thus avoiding process changes in bulk properties of the GaAs.

From Equation (1), with $N_c N_v = 5 \times 10^{36}/cm^6$, $p_p = 10^{17}/cm^3$, $D_n = 100\ cm^2/sec$, $\tau_n = 10^{-8}$ sec, and $T = 300°K$, one obtains

$$J_e = 3.2 \times 10^{-18} \left[e^{\frac{qV}{kT}} - 1 \right] A/cm^2.$$

If the heterojunction has much greater doping on the CdS side, the C-V characteristics would correspond to a step junction in the GaAs which is given by

$$C/A = \frac{0.85 \times 10^{-7} p_p}{V + V_o} \quad pf/cm^2 \tag{3}$$

where V_o is the built-in voltage

$$V_o = 1.4 - \Delta - V_F - V_F' \tag{4}$$

where V_F and V_F' are the positions of the Fermi level with respect to the respective band edges as shown in Figure III-7. These, in turn, are determined by the carrier concentrations of the materials and for non-degenerate materials:

$$V_F = kT/q \ln N_v/p_p \tag{5}$$

and

$$V_F' = kT/q \ln N_c'/n_n' \tag{6}$$

For example, setting $N_v = N_c' = 10^{19}/cm^3$ and taking $p_p = 10^{17}/cm^3$ for $n_n' = 5x10^{18}/cm^3$, we find that $V_F' = 0.018v$, $V_F = 0.12v$, and $V_o = 1.06v$ if $\Delta = 0.2$ eV.

Some preliminary experimental results are available on these heterojunction diodes, and a typical diode from sample 54-24-1 will now be described. A p-type GaAs wafer ($\rho = 0.23$ Ωcm, $p_p = 1.5x10^{17}/cm^3$) was lapped and mechanically polished. Ohmic contacts were made to the back. The front (As side) was cleaned and chemically polished with 3 parts H_2SO_4, 1 part H_2O, and 1 part H_2O_2. Mesa dots of CdS of 0.0137" diameter were evaporated using 850°C boat temperature and 120°C substrate temperature. The CdS source material was doped n-type to the composition 0.5 molecules In_2S_3 to 100 molecules CdS. The evaporated layer was 8μ thick and had $\rho = 0.00137$ Ωcm. Ohmic contacts to the CdS were made with 0.006" diameter evaporated In dots.

The capacity voltage characteristic of one of these diodes is shown in Figure III-8 as $1/C^2$ vs. V. The data could be fitted by a straight line, as expected for constant p_p, and gave an intercept $V_o = 1.1$ volts. Since the CdS is degenerate $V_F' \approx 0$, and $V_F = 0.11$ eV from Equation (5). This gives $\Delta = 0.19$ eV from Equation (4), which is what we expected from the χ of GaAs and CdS in contact to Au. The zero-bias capacity calculated from Equation (3) is 115 pf and compares quite well with the measured value of 126 pf.

The V-I characteristics of this diode are shown in Figure III-9. These, however, do not agree with the V-I char-

acteristics of injected carriers as given by Equation (1). The experimental curve is of the usual form

$$I = I_s[e^{qV/nkT}-1]$$

where $I_s = 6\times10^{-11}$A and n = 1.33. From Equation (1) the I_s should be about 3×10^{-21}A, so the diode current is completely dominated by a mechanism of current flow other than injection of electrons into the bulk of the GaAs. Three possibilities for this excess current are: (1) injection of holes into states within the CdS or the GaAs-CdS interface which subsequently recombine with electrons; (2) recombination of injected electrons in the depletion region of the GaAs; or (3) leakage current around the perimeter of the CdS diode.

The first possibility seems unlikely on the basis of the magnitude of I_s. Injection of holes into CdS cannot cause an I_s larger than that corresponding to the flow of holes over the observed barrier (1.21 eV), with infinite recombination rate (or perfect sink) at the edge of the barrier. This current is given by

$$I_s = AqN_v v_o \exp[-1.21q/kT] = 4.4\times10^{-15} \text{ amp}$$

for an average thermal velocity $v_o = 10^7$cm/sec and $N_v = 10^{19}/cm^3$. Mechanisms (2) and (3) remain possible and experiments are planned which will test each of these suggestions. Very faint el emission was observable at 60 ma in this diode, but no efficiency measurement was possible.

The diode described above is typical of diodes in that set and is very similar to those on other wafers where the same type of CdS evaporation was made. Improved techniques of CdS evaporation are now being used, however, and diodes made of this material will soon be examined.

III.4. Effects of Doping on Photon-Optical Phonon Interaction in GaAs

III.4.1. Introduction

In our First Interim Engineering Report, we have discussed the possibility that phonons assist luminescent transtions and give rise to fine structure in the GaAs 1.37 eV emission spectrum shown in Figure 33 of that report. In order to correlate the various optical phenomena in GaAs, we have made a survey of wide regions of its absorption spectrum for variously doped samples. Among the spectral regins surveyed, the 32-38 micron region showed striking effects of doping. The Perkin-Elmer grating instrument described in Chapter V was used in this study.

The anomalous dispersion region resulting from the optical activity of the optical lattice vibrations has been studied in GaAs by Picus, Burstein, Henvis and Hass[19] who have calculated the transverse and longitudinal optical phonon energies to be 0.0332 eV and 0.0352 eV, respectively. The optical activity of these GaAs phonons (referred to as restrahlen bands) has also been studied by Cochran, Fray, Johnson, Quarrington and Williams[16] who observed exceedingly strong absorption coefficients (from 1300 to 1600 cm^{-1}) for four bands

located at 0.0331, 0.0340, 0.0355 and 0.0367 eV and a weaker band having an α of 400 cm^{-1} at 0.0391 eV. They also reported that a not easily reproduced fine structure of three to four fine peaks in each of the bands. Furthermore, they found the transmission through their samples to be essentially independent of thickness in the range of 14-68μ. While they did not claim an explanation for these results, they expressed the belief that the vibrational spectrum near k = 0 becomes dependent on the size and shape of specimens.

We have extended the observation of these "restrahlen" bands to GaAs samples having various carrier concentrations. We have used undoped n-type GaAs having electron concentrations from $1.8 \times 10^{15}/cm^3$ to $1.4 \times 10^{17}/cm^3$ and differently doped GaAs with charge carrier concentrations varying from $4.8 \times 10^{17}/cm^3$ to $1.1 \times 10^{19}/cm^3$. Some of our data on the strong bands were obtained by reflection. This was necessitated by free carrier absorption reaching a 1100-6000 cm^{-1} at that frequency over the doping range used[17] and a relatively weak source of far-infrared radiation.

III.4.2. Results

Figure III-10 shows the reflection spectrum that we obtained using an n-type GaAs specimen with a carrier concentration of $1.6 \times 10^{16}/cm^3$. It is seen that we have found the same five absorption bands reported by Cochran and coworkers,[16] although somewhat displaced (<0.0003 eV). We have also obtained a transmission spectrum (see Figure III-11) from a specimen of

the same starting material over a wider spectrum and noticed the presence of three relatively weak ($\alpha<30$ cm^{-1}) combination bands (LA+LA, LA+LO AND LA+TO) also described by Cochran and coworkers.[16] In all but one of the seven samples of undoped n-type GaAs studied, we have seen the restrahlen absorption bands. The sample which did not exhibit this absorption had the highest concentration (1.4×10^{17}/cm^3). In no case did we see the restrahlen absorption bands in samples doped with Zn, Cd, Mn or Sn (concentrations above 4.8×10^{17}/cm^3). This should be contrasted with the presence of the LA+ combination bands observed in a Cd doped material containing 2.4×10^{18} holes/cm^3 where, however, all the restrahlen bands were missing. (See Figure III-11.)

We have also obtained the absorption spectrum of undoped 1.2×10^{16}/cc GaAs by direct transmission in the 39 to 45 millielectron volt range, using the grating spectrophotometer. The result of correlating our transmission data, for two samples of the same material, is shown in Figure III-12, along with a plot of the absorption coefficient, α, reported by Cochran, et al.[16]

Three main bands were found in this region by these workers and were labeled as combination bands, involving the transverse acoustical phonon with $\alpha\sim25$-150 cm^{-1}.

The band at 0.038 eV was attributed by Cochran to the LO+TA combination and the bands at 0.0398 and 0.0413 eV to the TO_1+TA and TO_2+TA combinations.

Our data shows several strong absorption peaks in

addition to the three found and labeled as combination bands by Cochran. We place their three strong peaks at 0.0384, 0.0402 and 0.0415 eV, and in addition, find a peak at 0.0407 eV, where they have none, and a broad pair of peaks at 0.0435 and 0.0444 eV. We were able to resolve the absorption "shoulders" on their peaks into distinct satellite peaks, as seen in Figure III-12, and even these peaks have a fine structure of their own. The positions of these satellite peaks at 0.0444, 0.0448, 0.0421, 0.0426, 0.0395, and 0.0389 eV agree well with the positions of the shoulders on Cochran's main peaks.

It is clear from Figure III-12 that a large amount of splitting up into a finely structured series of peaks takes place within the 0.039 to 0.045 eV range. This was also observed by Cochran, et al, but they were unable to reproduce this structure.

III.4.3. Discussion

Our 32-38 micron results indicate that complete masking of the restrahlen bands by free carrier absorption is most unlikely for at least the lower concentrations of the doped GaAs samples and that another explanation for their absence has to be provided. It is proposed that the size and shape dependence and defect coupled disappearance of the GaAs restrahlen have a common cause. Furthermore, the introduction of more than 10^{17} defects into GaAs destroys the long range coherence of the k = 0 phonons (i.e., those phonons which are to be found at the center of the Brillouin zone and which have

very long wavelengths). Thus, it is not anymore possible to absorb photons at this energy, since k = 0 ceases to be a "good quantum number".

We shall now return back to the discussion of the absorption and emission spectrum in GaAs. We refer to Figure 36 and Section 3.1.1.3. on pages 40 and 41 of our First Interim Engineering Report. There we have pointed out the anomaly in Region II (from $3x10^{17}$ to $3x10^{19}$ carriers/cm^3) over which we observed a widening, i.e., blue shift, of the absorption edge by approximately 0.020 eV when measured for $\alpha \sim 10$ cm^{-1}. We have further stated that the energy band structure of GaAs is fairly well established as having a k <000> conduction band minimum and "direct" optical transitions. However, we have then erroneously added that phonon assisted direct transitions are forbidden. In fact, Bardeen, Blatt and Hall[18] who discussed indirect transitions showed that phonon assisted transitions are quite common and explained fully the apparently anomalous optical absorption spectrum of germanium and silicon. There appears to be no reason why k = 0 phonons could not assist absorption and emission in GaAs. If they did, and if they also disappeared above a certain doping concentration, this could explain the shift of the absorption edge with doping, as referred to above. It could also explain the nature of the near edge electroluminescence spectrum in GaAs and may further shed light upon the temperature dependence of el efficiency in GaAs.

Thus, it would follow that at temperatures below

350-430°K, phonon assistance would be predominately phonon emission. This would enhance absorption for energies 0.033 to 0.039 eV above the band edge and/or enhance emission below the band edge. It would thus provide a natural window for el light to escape from the GaAs. Both heating and heavy doping (above $10^{17}/cm^3$) would tend to destroy this "transmission window" effect.

Currently, we are carrying out further experiments to test the "window hypothesis" which appears to be consistent with a large array of data on IR absorption, near edge absorption and emission and el efficiency dependence on doping and temperature.

III.5. BP Injection Luminescence

Since only during the last week of the period covered by this report, sizable cubic BP crystals have been available, and since ohmic contacts to BP still offer some technological difficulties, our results are rather preliminary.

Two types of boron phosphide crystals are now available for experimentation. The first type is cubic and most likely contains an excess of phosphorous (see Chapter V of this report and Section 3.1.2. of the First Interim Engineering Report). These crystals emit orange-red and sometimes blue (depending on the color of the BP crystals themselves). The second type of boron phosphide has a rhombohedral structure and a chemical composition in the range between $B_{13}P_2$ and BP.[21] Even these crystals emit visible electroluminescence when contacted

with W, Ni or Au electrodes at currents that are less than 20 ma. Visible light emission from such a BP diode has been studied and a preliminary spectral analysis made with the Beckman DK-2 spectrophotometer. Figure III-13 shows the BP emission vs. wavelength for a 160 ma pulse of 6.5 msec width, at a pulse repetition rate of 500 pps. Two well-separated emission peaks are present at 425-440 mμ (2.92-2.82 eV) and at 560 mμ (2.22 eV), with half widths of 420Å and 900Å, respectively.

Very weak cathodoluminescence was also observed in BP by bombarding a small chip mounted on the front face of a cathode ray tube with a 2.8 KeV electron beam. The chip appeared to luminesce with both a deep purple-blue color and a pink color, reminiscent of our injection electroluminescence observations.

Transmission measurements and further el observations on BP are anticipated in the near future using the larger single crystals prepared recently in this laboratory

REFERENCES (Chapter III)

1. J.I. Pankove and M. Marsonlie, J. Electrochem. Soc. 11, 71 (1962).

2. R.J. Keyes and T.M. Quist, Proc. IRE 50, 1822 (1962).

3. -hpa-, First Interim Engineering Report, Contract No. AF33(657)-9772.

4. C.S. Fuller and M.J. Whelan, J. Phys. Chem. Solids 6, 173 (1958).

5. J.T. Edmonds, J. Appl. Phys. 31, 1428 (1960).

6. J.J. Wysocki, J. Appl. Phys. 31, 1686 (1960).

7. R.N. Hall and J.H. Racette, Final Report, Scientific Report No. 8A, Contract AF19(602)-6623, Project 4608, Task 46088, May 31, 1962.

8. J. Blanc, R.H. Bube and H.E. MacDonald, J. Appl. Phys. 32, 1666 (1961).

9. J. Blanc, R.H. Bube, and L.R. Weisberg, Phys. Rev. Ltrs. 9, 252 (1962).

10. Spectrographic Analysis, performed by G. Marshall of this laboratory.

11. M.I. Nathan and G. Burns, Appl. Phys. Ltrs. 1, 89 (1962).

12. M.I. Nathan and G. Burns, Bull. Amer. Phys. Soc. Abstract, p. 201, Junction Luminescence Meeting, St. Louis, March 25-28, 1962.

13. T.S. Moss, J.A.P. 32, 2136 (1961). Moss and Hawkins, Infrared Phys. 1, 111 (1961).

14. W.P. Dumke, Bull. Amer. Phys. Soc., Abstract, p. 201, Junction Luminescence Meeting, St. Louis, March 25-28, 1962

15. I. Kudman and T. Seidel, J. Appl. Phys. 33, 771(1962).

16. W. Cochran, S.J. Fray, F.A. Johnson, J.E. Querrington, an N. Williams,"Lattice Absorption in GaAs," J.A.P. Supplm. to Vol. 30, No. 10, 2102 (1961).

17. W.G. Spitzer and J.M. Whelan, Phys. Rev. 114, 1, 62, (1959).

18. J. Bardeen, F.J. Blatt and L.H. Hall, Atlantic City Photoconductivity Conference, 146, November 4-6, 1954, John Wiley (1956).

19. Picus, Burstein, Henvis and Hass, J. Phys. Chem. Solids, 8, 282 (1959).

20. Hall, Racette and Ehrenreich, Phys. Rev. Ltrs. 4, 456 (1960).

21. L.H. Spinar, Acta Cryst. 15, 1048 (1962).

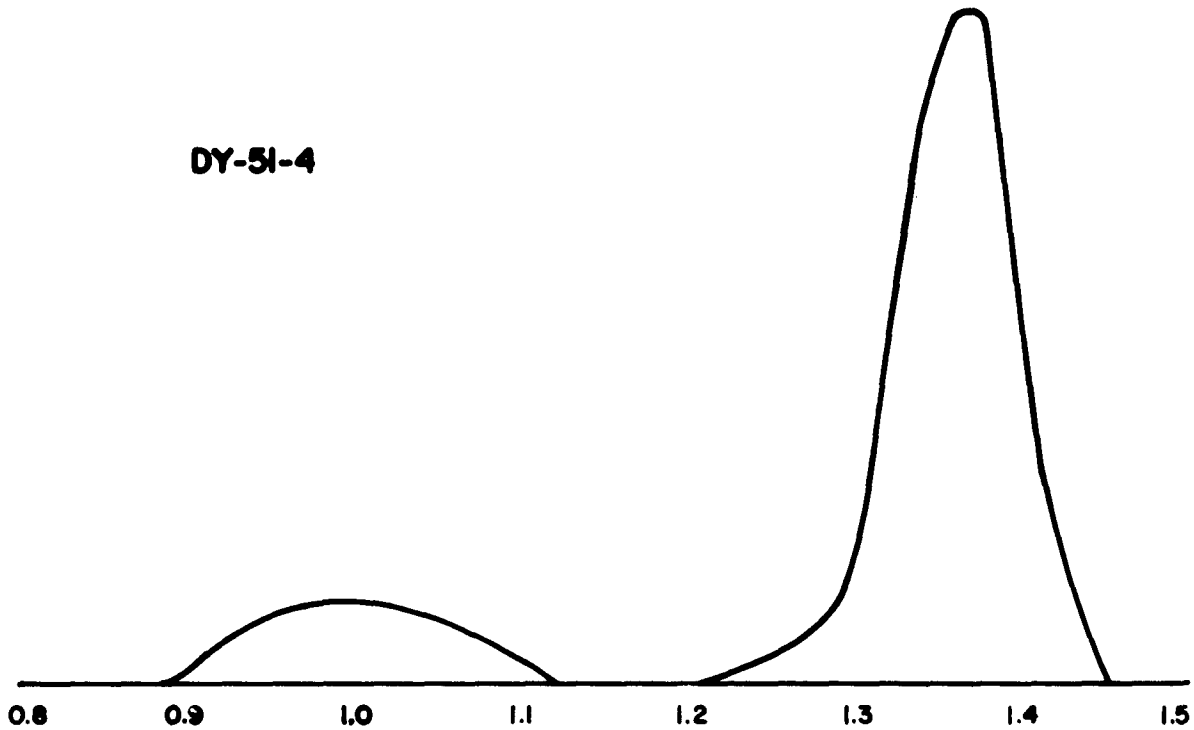

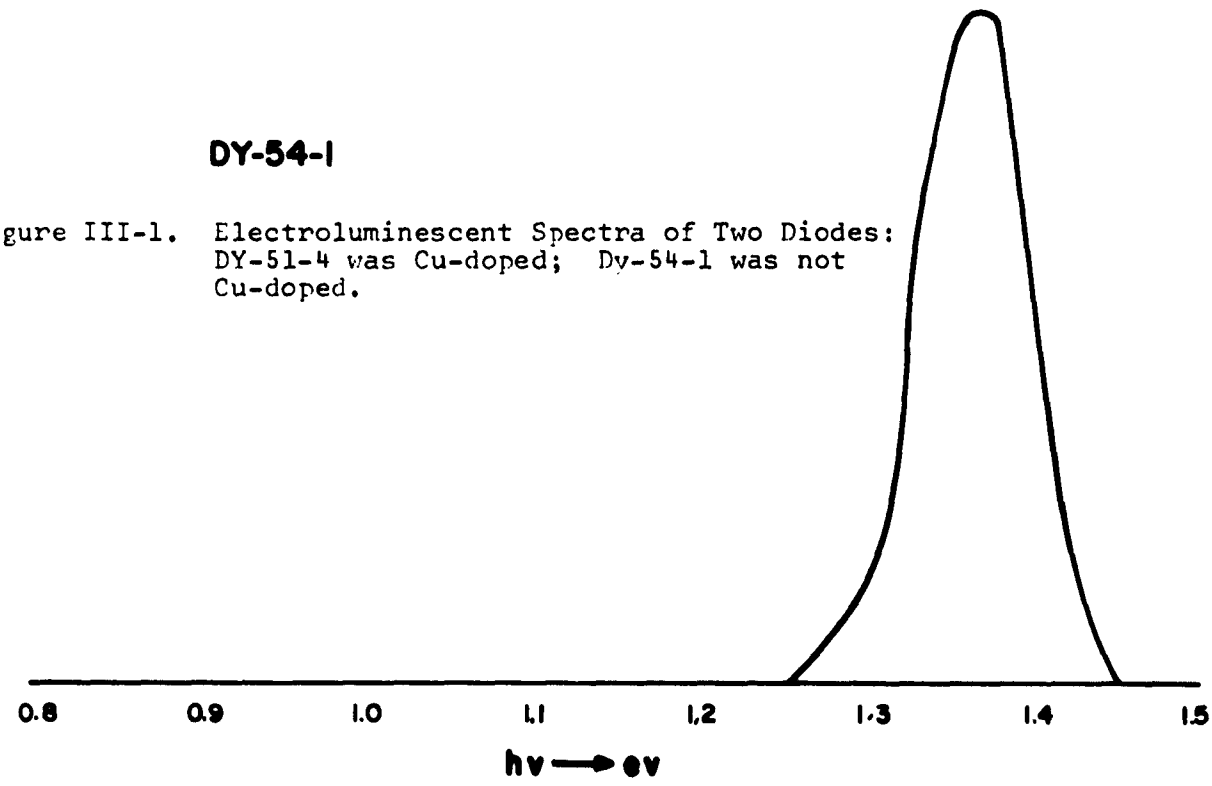

Figure III-1. Electroluminescent Spectra of Two Diodes: DY-51-4 was Cu-doped; Dy-54-1 was not Cu-doped.

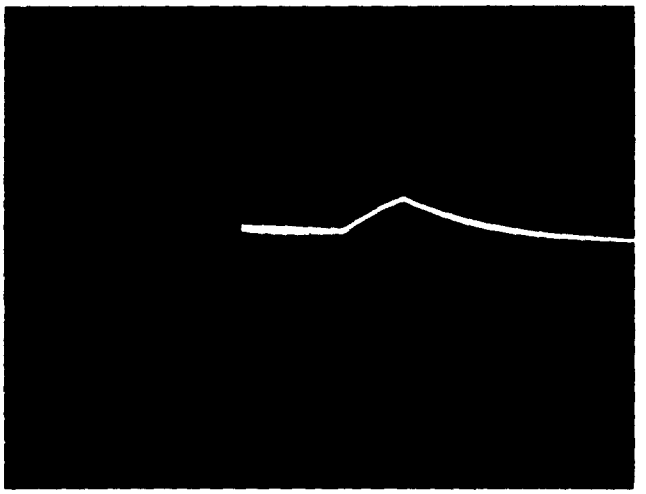

Figure III-2. Photomultiplier Pulse Output Used for Synchronous Sampling.
Vertical Scale: 20 mv/cm
Horizontal Scale: 20 μsec/cm
Diode Current Pulse: 125 ma

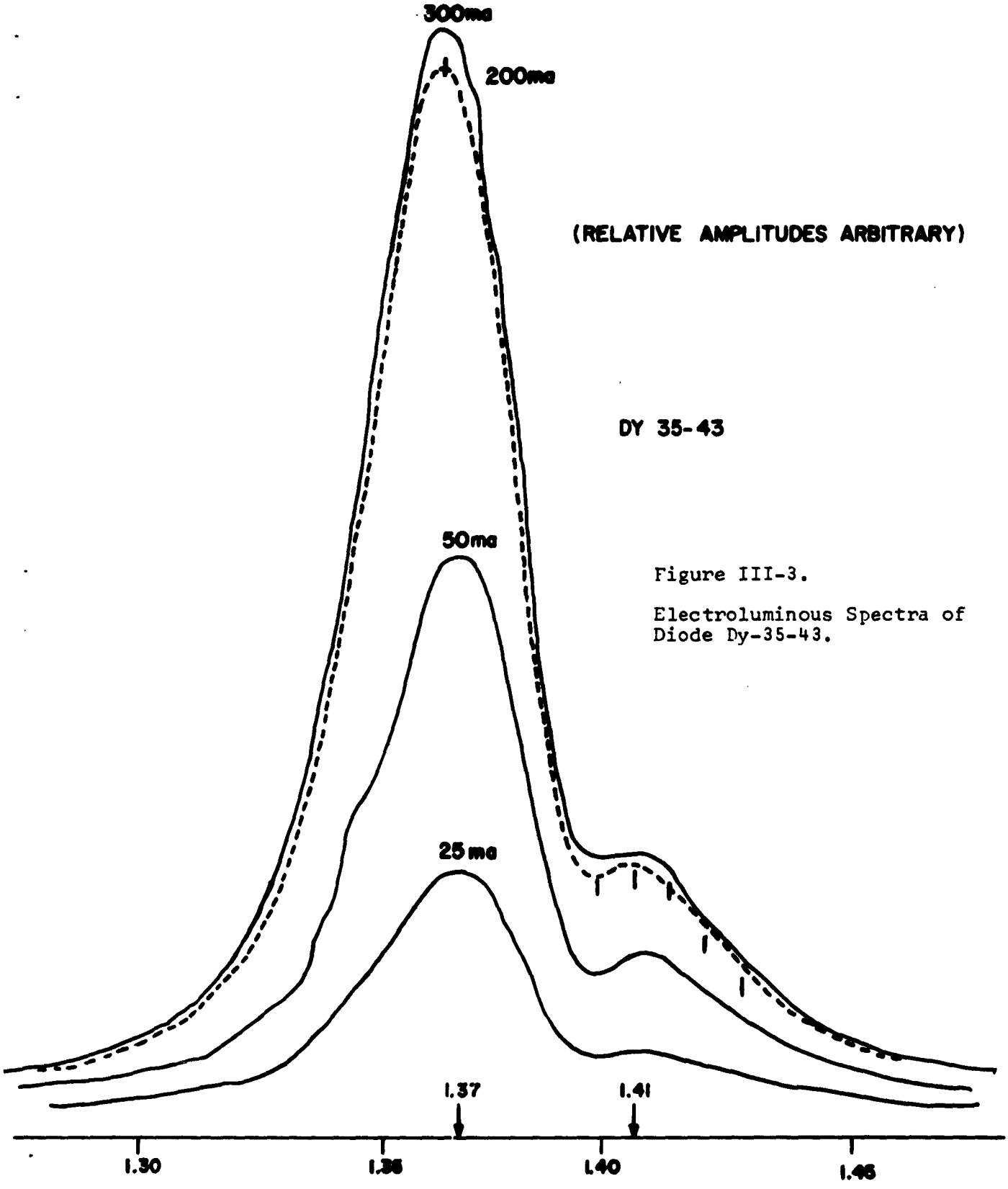

Figure III-3.

Electroluminous Spectra of Diode Dy-35-43.

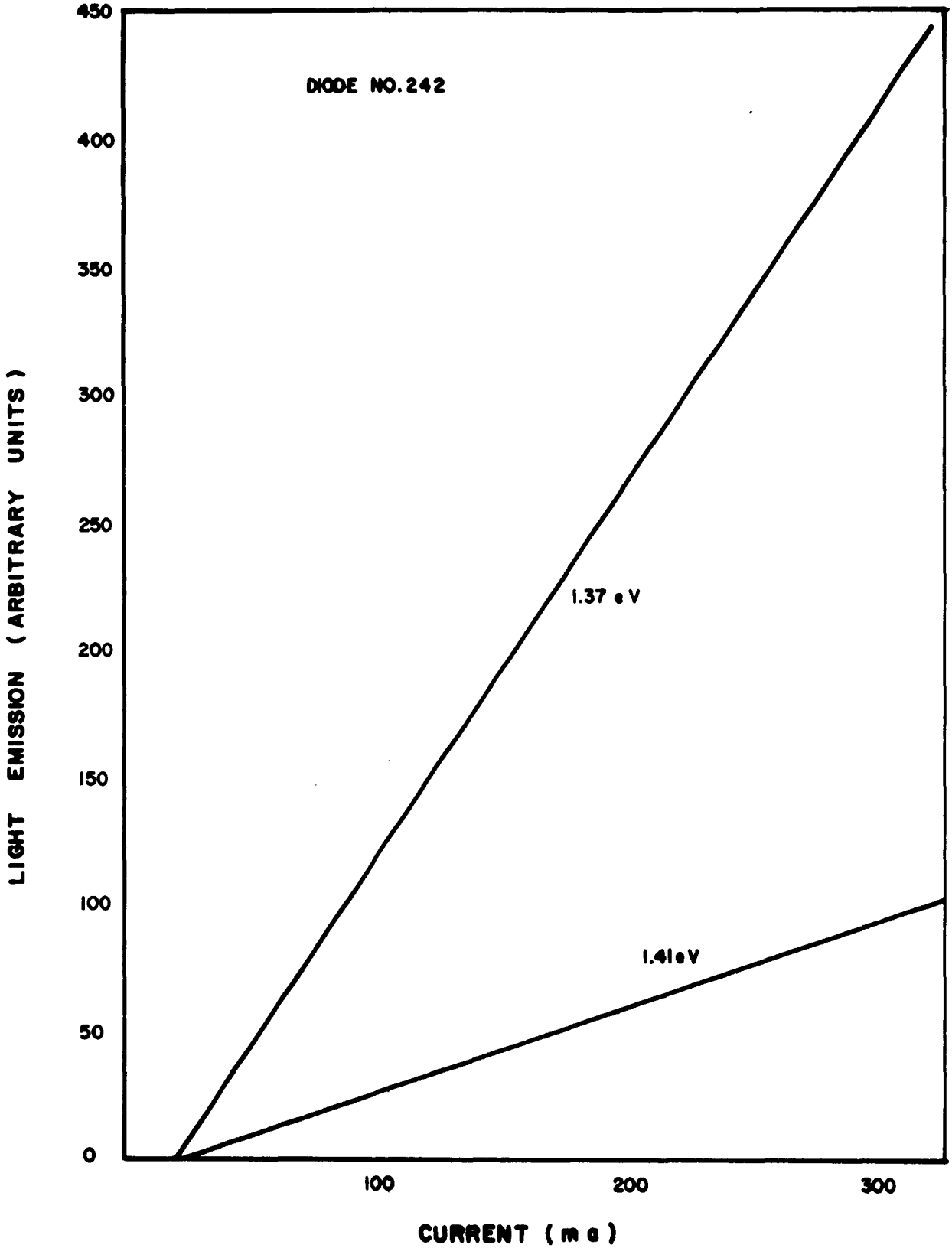

Figure III-4. Spectral Peak Amplitudes as a Function of Diode Current.

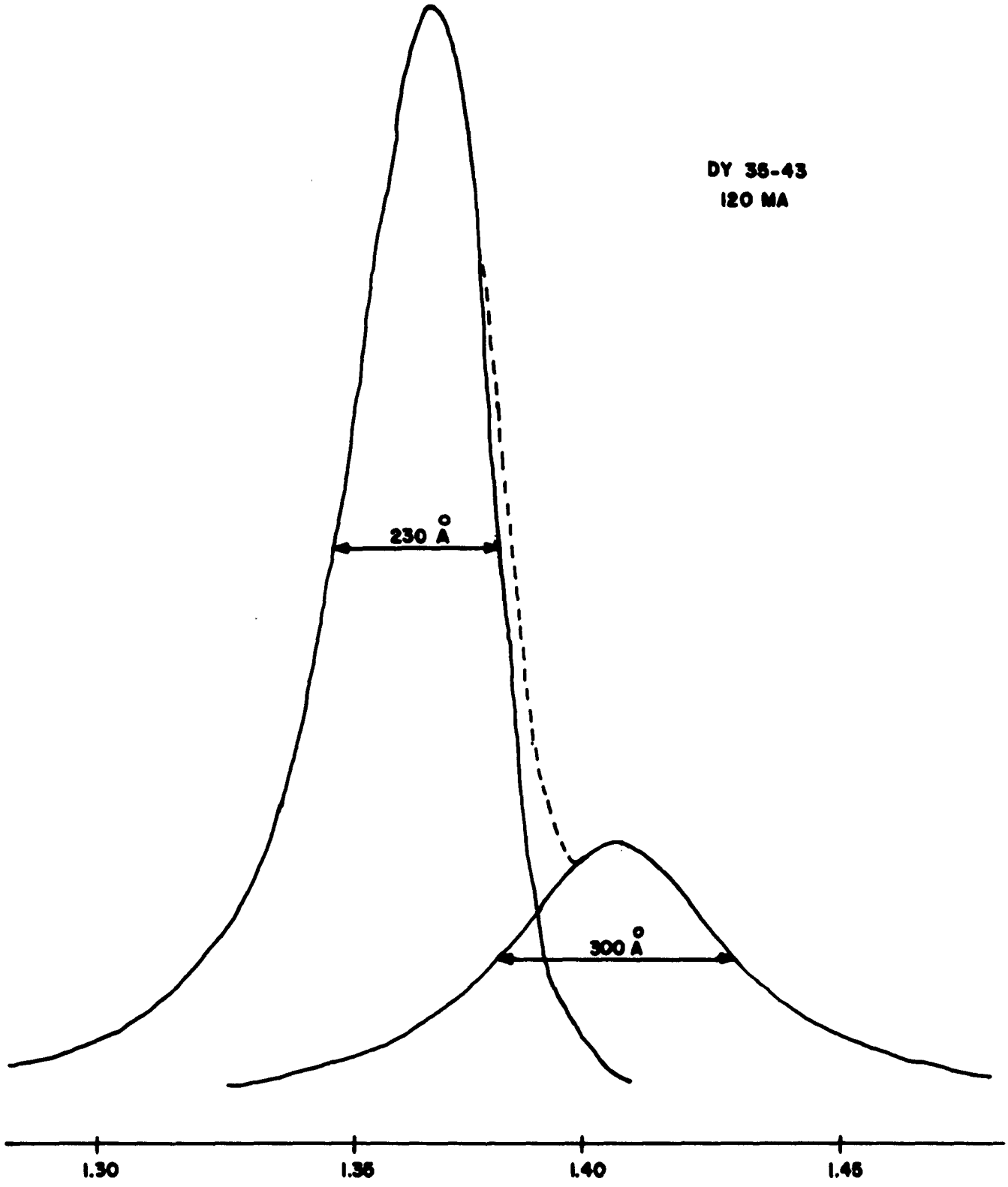

Figure III-5. Graph Showing Subtraction of the Two Edge el Peaks.

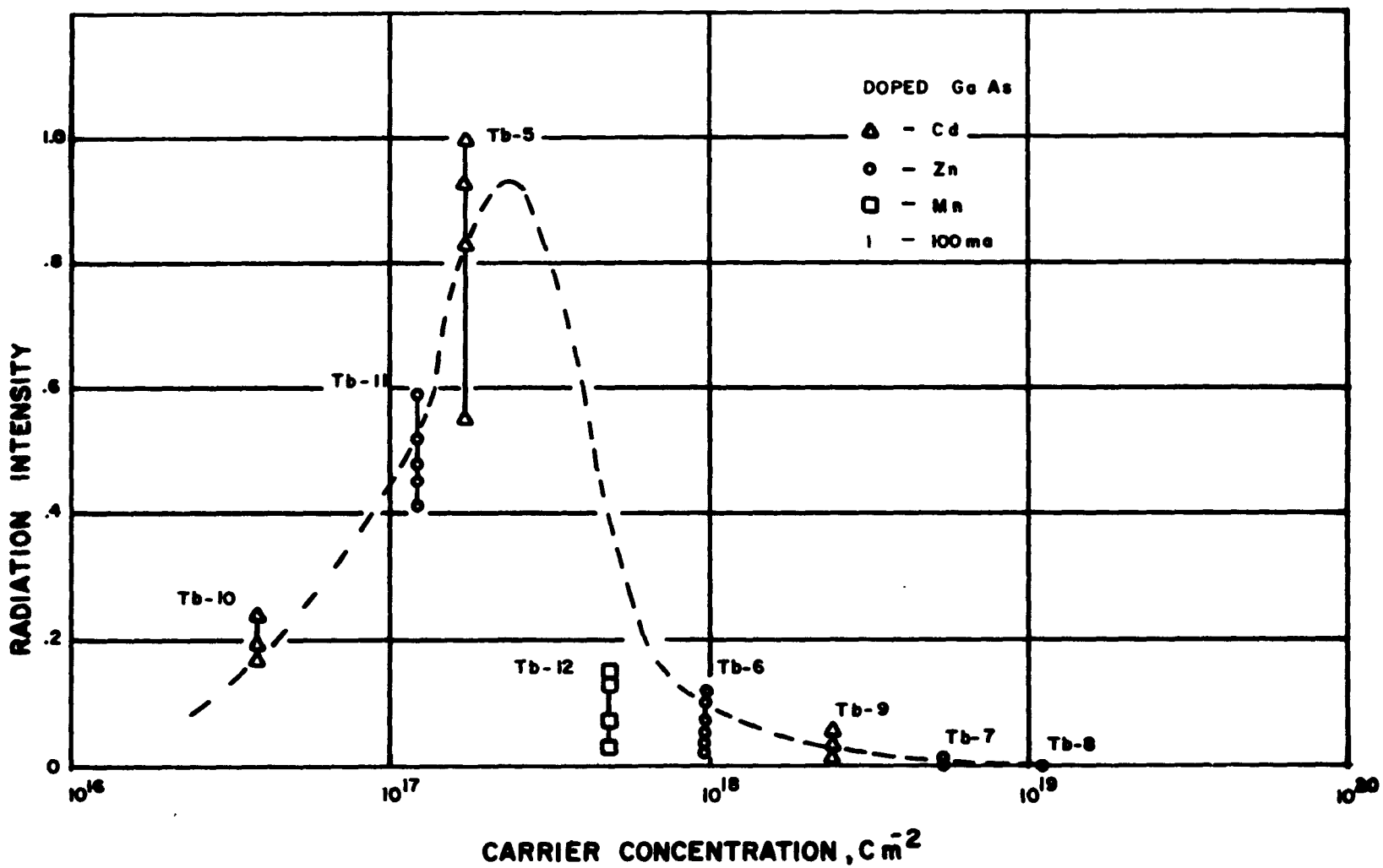

Figure III-6. Relative Electroluminous Emission Efficiencies as a Function of Whole Concentrations in p-Type GaAs.

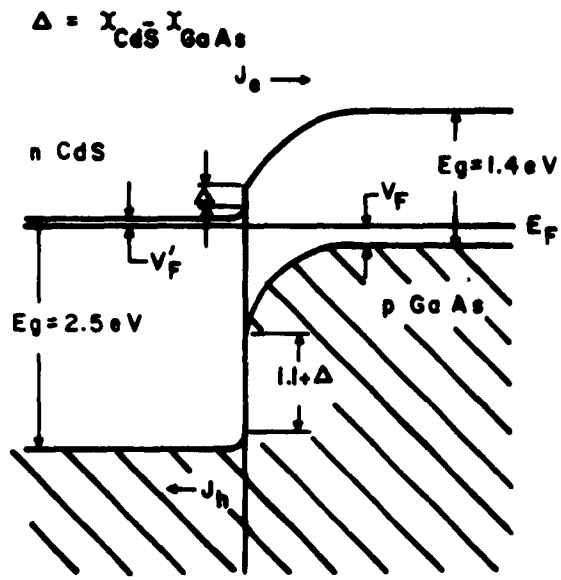

ELECTRON ENERGY DIAGRAM OF CdS-GaAs HETEROJUNCTION

Figure III-7.

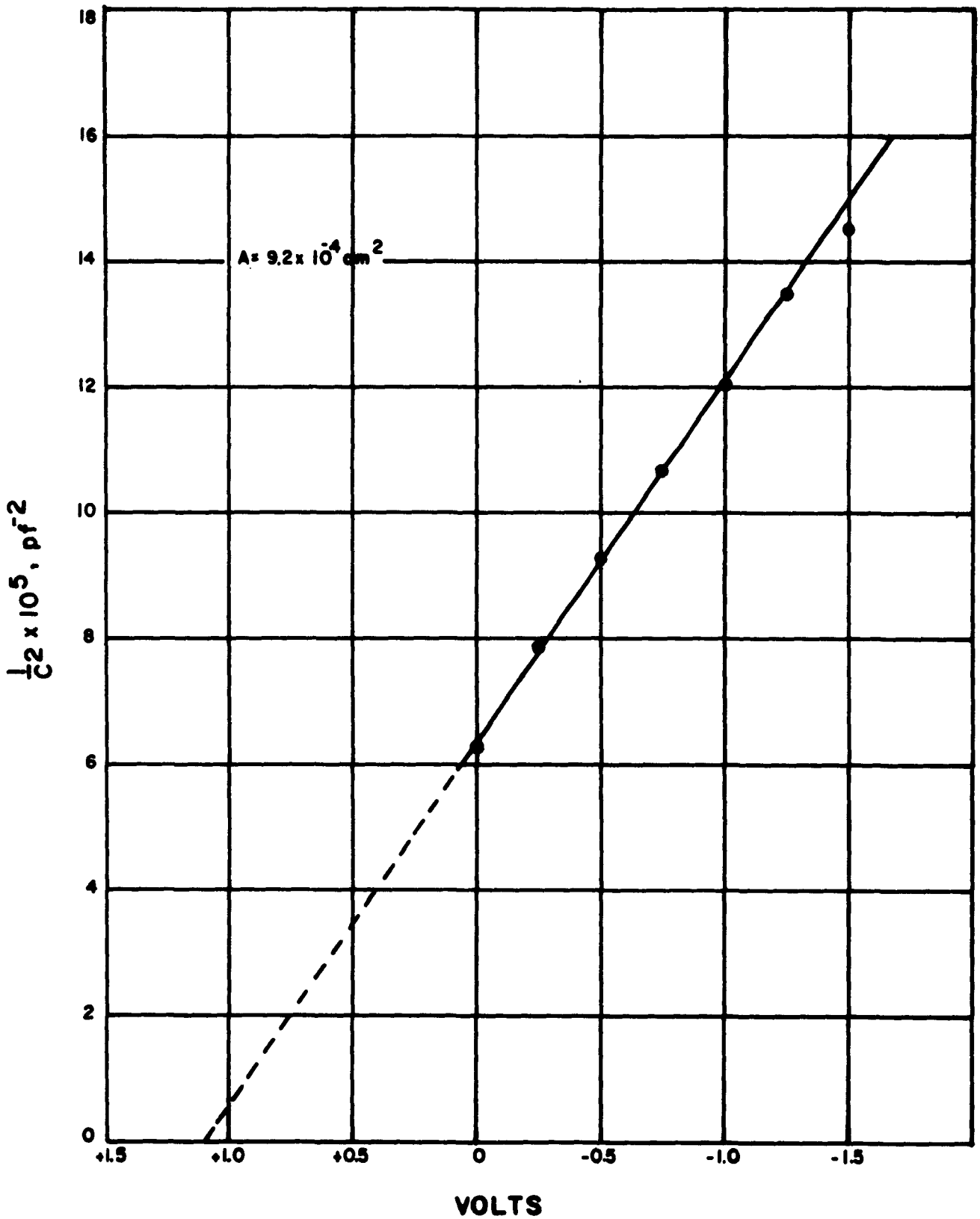

Figure III-8. Capacity-Voltage Characteristic of a CdS-GaAs Heterojunction Diode.

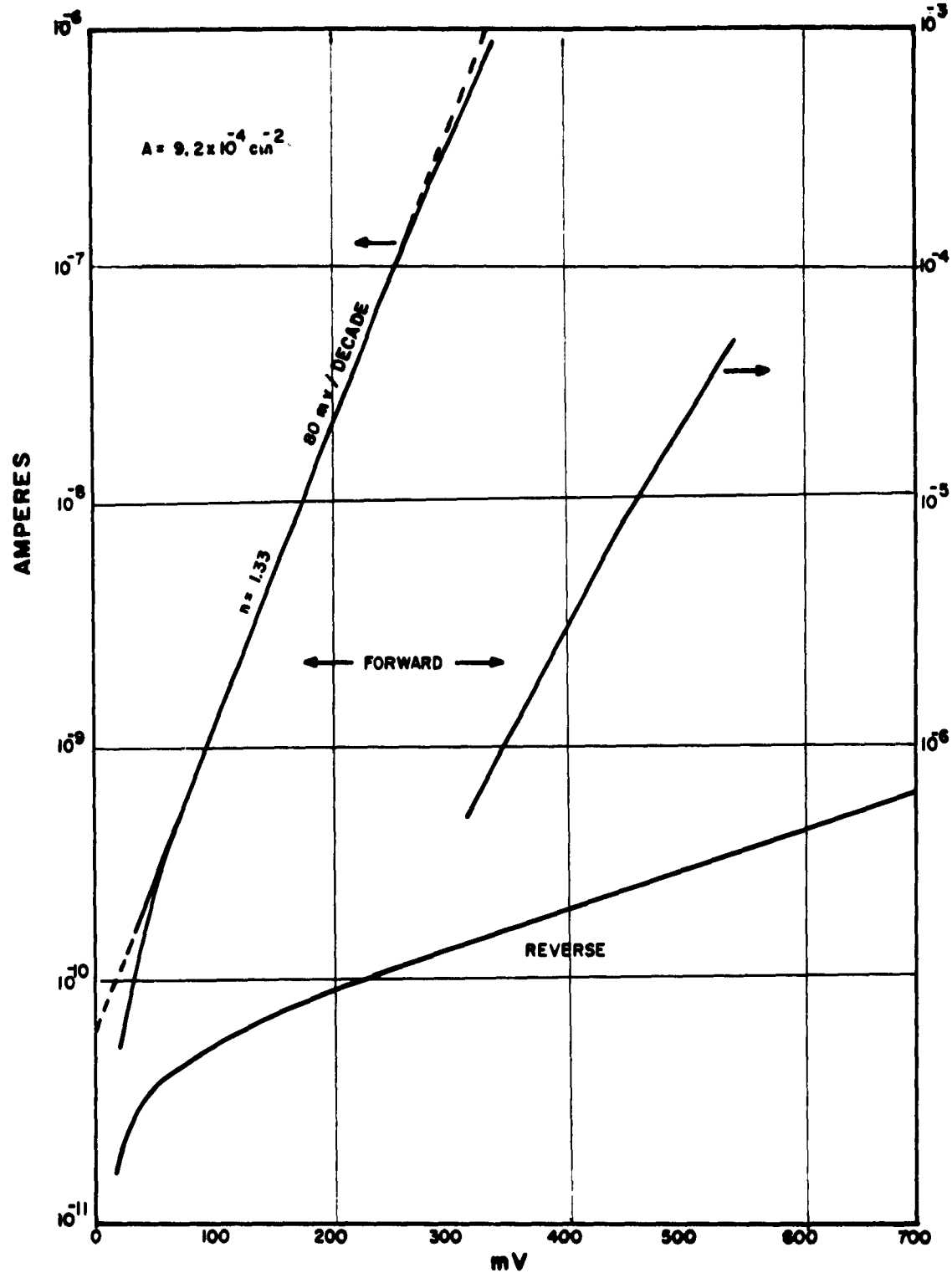

Figure III-9. V-I Characteristic of the CdS-GaAs Heterojunction Diode.

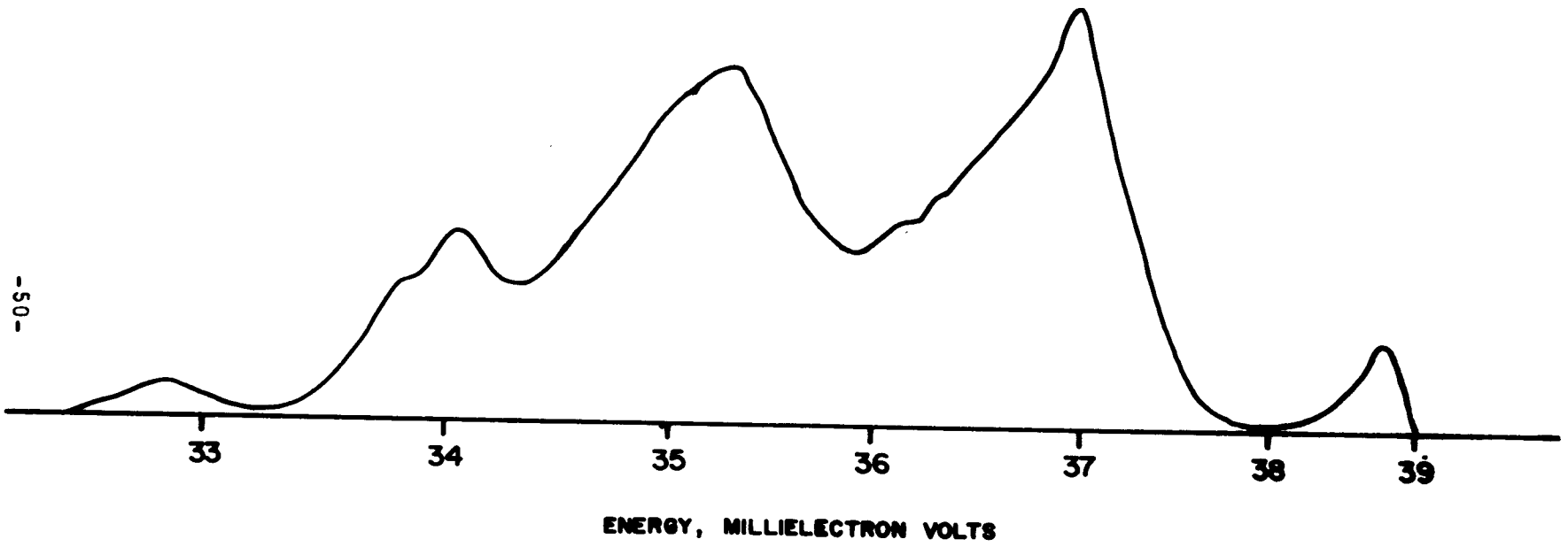

Figure III-10. The Reflection Spectrum of GaAs, n-type, Carrier Concentration $1.6 \times 10^{16}/cm^3$. These bands are referred to as "restrahlen bands".

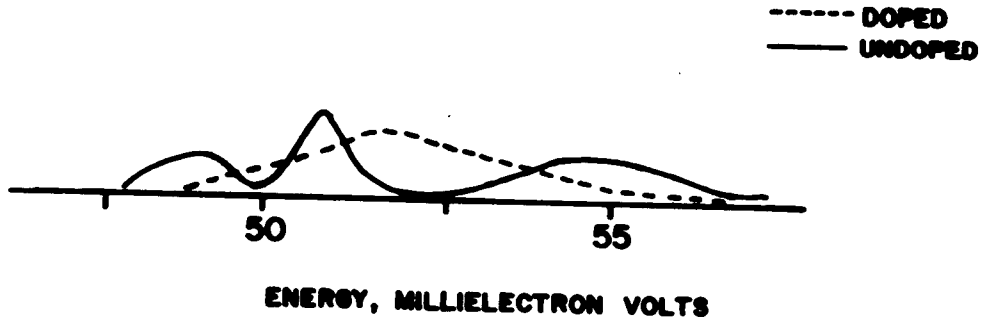

Figure III-11. Transmission Combination of GaAs, n-Type, Carrier Concentration $1.6 \times 10^{16}/cm^3$. These Bands Are Referred to as "Phonon Combination Bands"

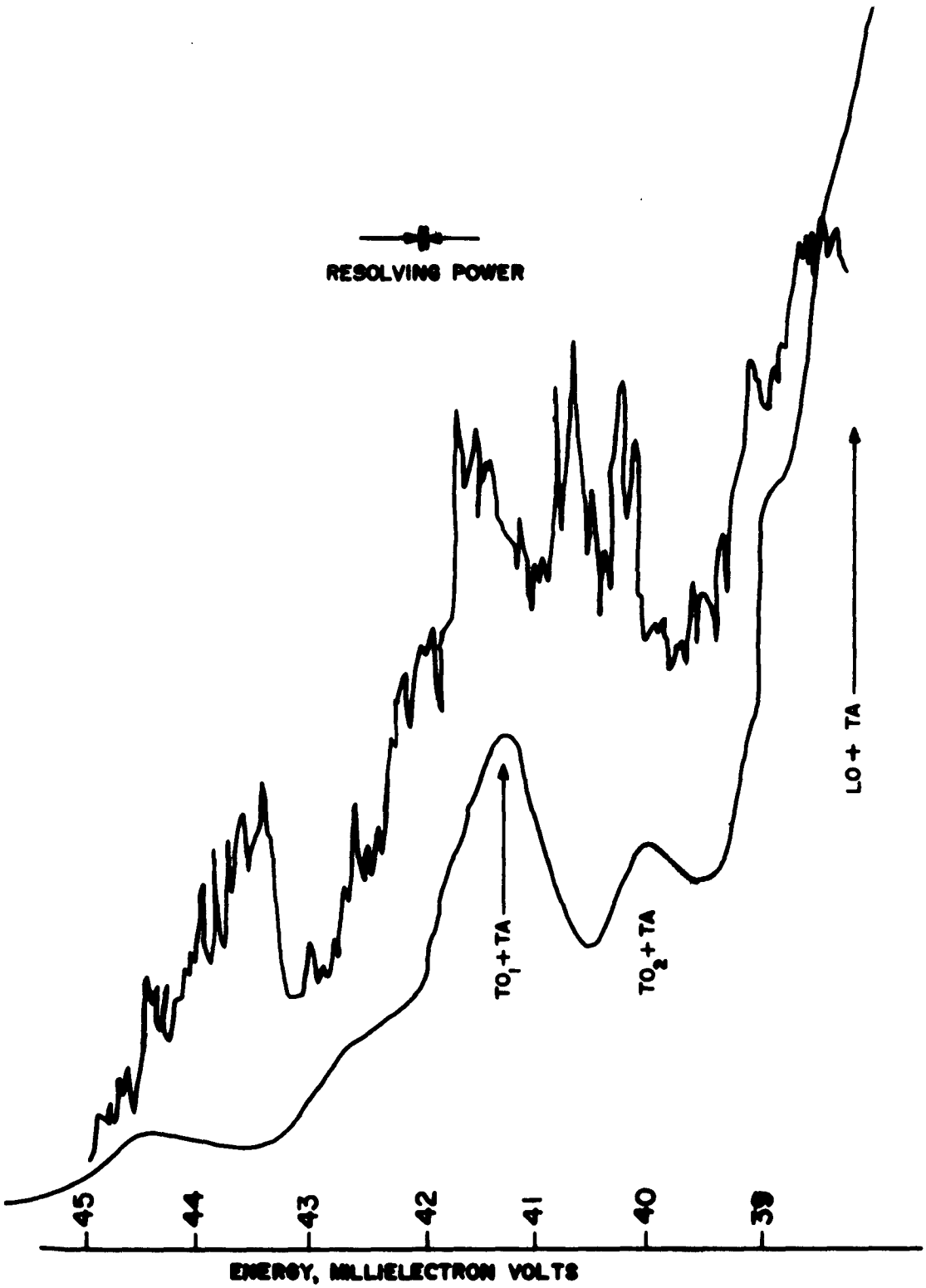

Figure III-12. Absorption Spectra of Undoped GaAs. Lower Curve is a Plot of the Absorption Coefficient Reported by Cochran, Ref. 16. Upper Plot is Our Data for GaAs, n-Type, Carrier Concentration 1.2×10^{16}/cc.

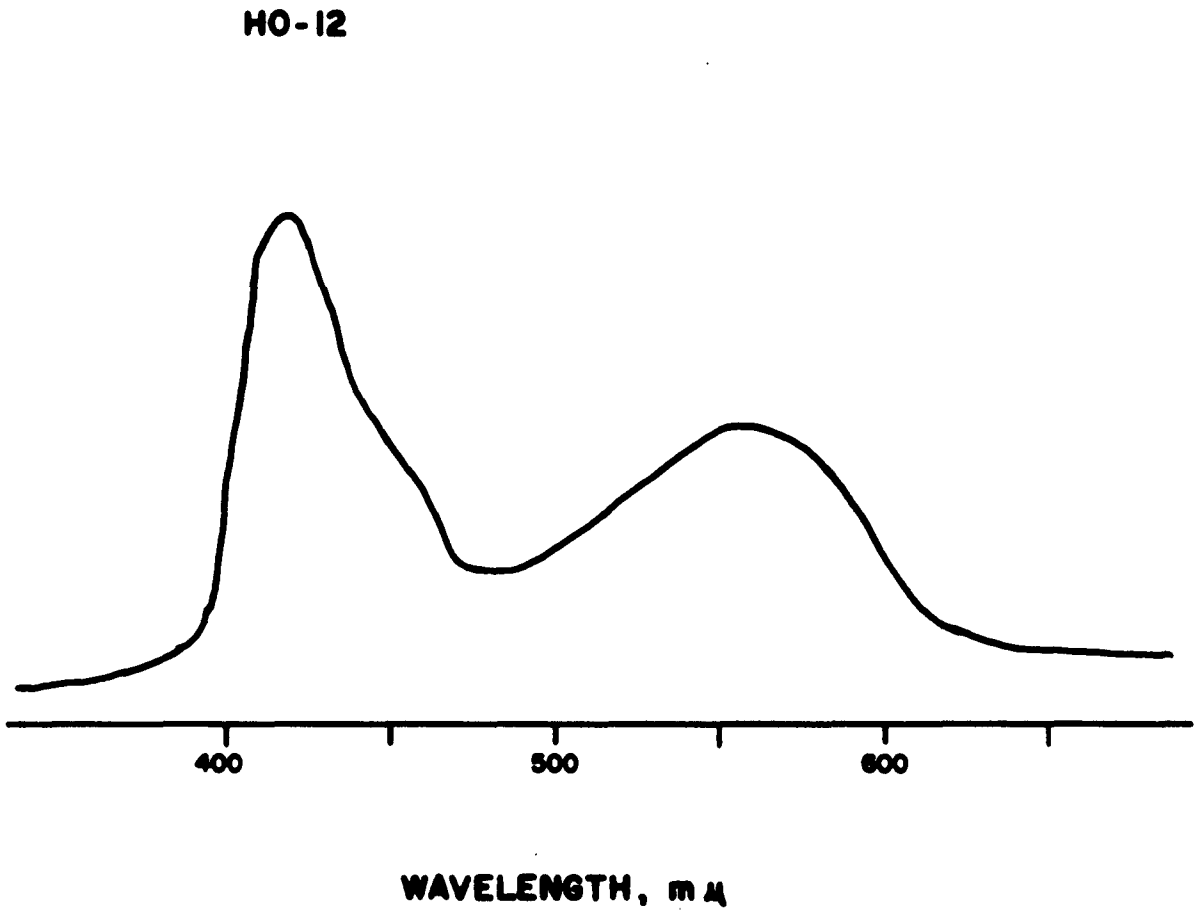

Figure III-13. Electroluminescent Emission vs. Wavelength for a Single Crystal Rhombohedral BP. Siode Current Pulse Amplitude: 160 ma; Pulse Width: 6.5 msec; Repetition Rate: 500 pps/sec.

CHAPTER IV

OPTOELECTRONIC PAIRS

A major problem in optoelectronic networks and functional blocks is an efficient transmission and interception of light linking the light emitting and light receiving parts of the networks.

In Figures IV-1 and IV-2, we show photographs of a standard mesa GaAs el diode under external and self-illumination, respectively. Both views were taken looking from the mesa side of the device. (Compare with Figures 6 and 7 of our First Interim Engineering Report.) It may be seen that the most intense radiation emitted upwards originated at the rim of the mesa and particularly in the vicinity of the gold ball contact. It is also interesting to note that a sizable fraction of the radiation is being reflected from the metal grid electrode on the opposite side of the GaAs chip. The photograph further indicates a focussing action at the inward edges of the square openings etched into GaAs between the electrode grid. The clarity of the reflected electrode image under infrared self-illumination of the GaAs device clearly demonstrates the high degree of transparency of the n-type base to the 1.37 eV light.

The spatial pattern of the light flux emitted by the diode was measured in an annulus whose plane was perpendicular to the plane of the junction. The results are shown in Figure

IV-3(a). Note that both the asymmetrical emission seen in Figure IV-2 and the presence of posts influence the radiation pattern. In Figures IV-3(b) and IV-3(c) are shown radiation patterns from other diodes of similar construction, but different electrode geometry. Diode in (b) had an Al grid on the mesa, while the diode in (c) had a mesa completely covered with an Al electrode. It is clear from the comparison of these two cases that the radiation pattern is profoundly affected by the electrode geometry.

In another experiment, we have constructed a GaAs el diode which has a prolonged mesa shape, as seen in the photograph in Figure IV-4 under self-illumination. As in the previous case, a high intensity radiation output originates at the rim of the mesa in the vicinity of the gold ball electrode contact. However, a significant radiative contribution emanates also from regions in the device where no current is expected to flow. This demonstrates the effect of el light piping and transmission through the diode base. The radiation pattern of this diode is seen in Figure IV-5. In contrast to the previous cases, this diode has a significant output tangential to the junction plane.

It was, therefore, concluded that the major contribution to the losses incurred in coupling el diodes to photosensors comes not from self-absorption but from geometrical optics and other geometrical factors. We have tested and confirmed

this conclusion with the setup shown in Figure IV-6. It permitted a three dimensional motion of both the el diode and the phototransistor and showed great variability in the current transfer ratio between the two devices as a function of their relative orientations.

The spatial emission pattern from GaAs el diodes was found to be profoundly influenced by imbedding the diode into a glass having an index of refraction of about 2.7. (See Chapter VI.) However, the total light output into the surrounding air was not appreciably changed. This was probably due to optical mismatch between the glass and the air. Similar tests were carried out on silicon phototransistors. Glass imbedment reduced their photosensitivity by about 25-50%.

The above experiments are preliminaries in our program of developing the best optical match between el diodes and photosensors. The work has just begun and it is not sufficiently advanced to be reported in detail at this time. At present, our preliminary tests indicate that air coupled pairs of el diodes and photoconductors utilize about one-sixth to one-eigth of the light which may be utilizable under optimum optical conditions.

Figure IV-1. Photomicrograph of a "Standard" Mesa Zinc Diffused GaAs el Diode. (External Illumination.)

Figure IV-2. Photomicrograph of Diode in Figure IV-1 Under Self-Illumination.

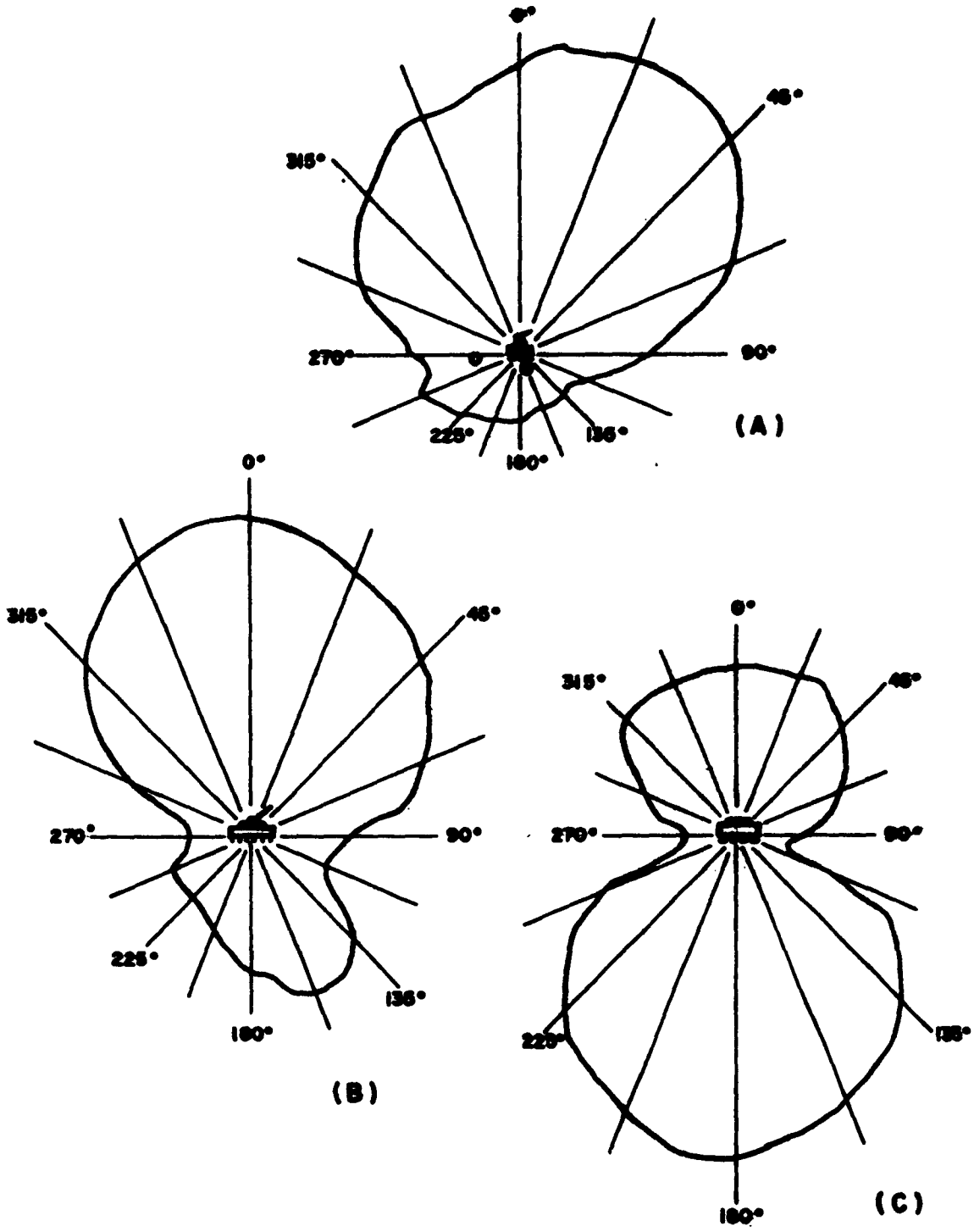

Figure IV-3. Radiation Patterns of Zinc Diffused Mesa el GaAs Diodes. (a) Pattern of Diode in Figures IV-1 and IV-2; (b) Similar Diode With Al Grid on Mesa; (c) Similar Diode With Black Mesa.

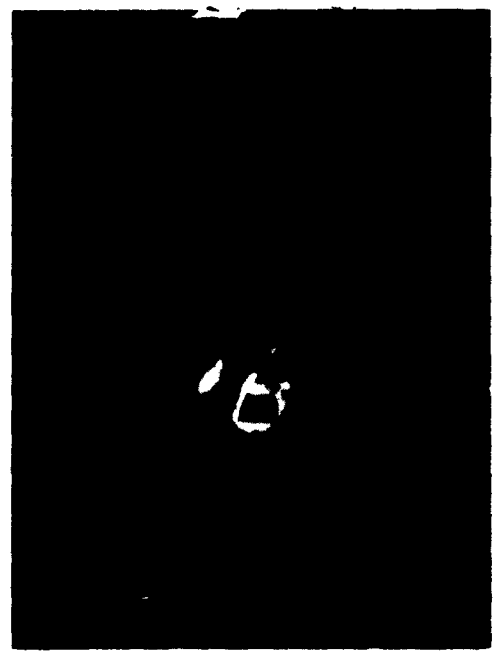

Figure IV-4. GaAs Zinc Diffused el Diode Having a Prolonged Mesa Under Self-Illumination.

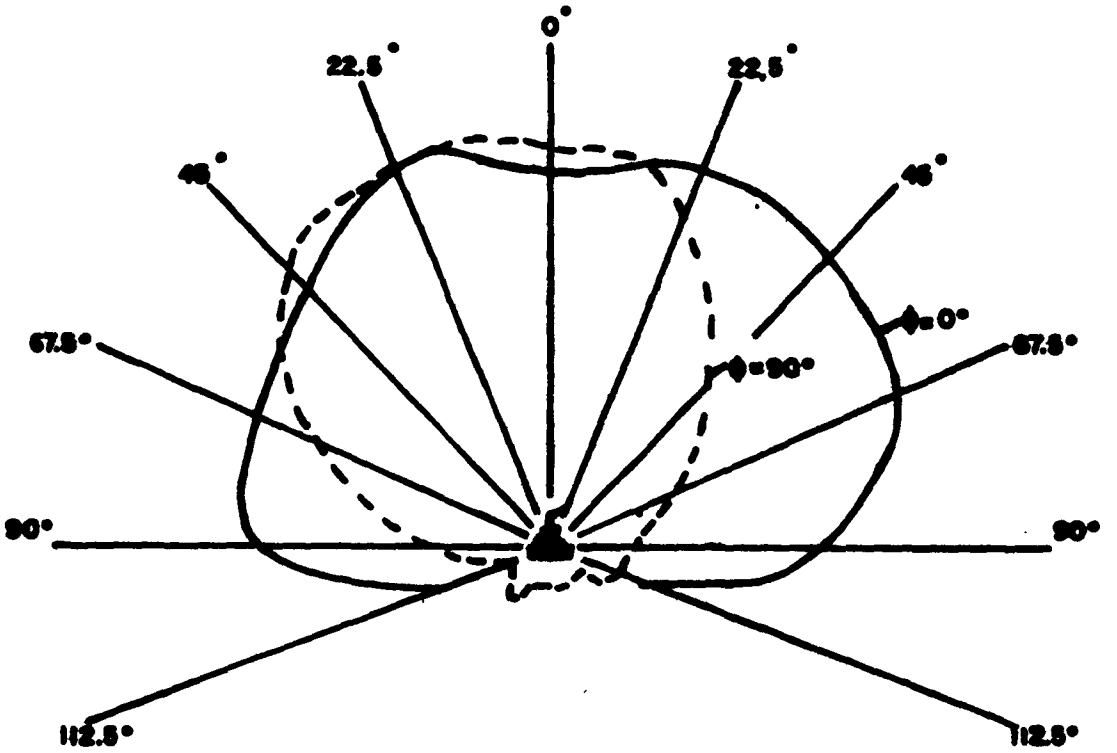

Figure IV-5. Spatial Radiation Pattern of el Diode From Figure IV-4.

CHAPTER V

INSTRUMENTATION

V.1. Thermoelectric Power Supply

A power supply was required which would furnish an easily controlled dc excitation from 0 to 50 amperes and yet have less than 1% ripple. This low ripple was required in order to achieve the ultimate cooling capability of the peltier junction, since ac excitation components produce heat without any net heat pumping action.

The circuit is shown in Figure V-1. This power supply departs from conventional ones in that a high leakage reactance is deliberately introduced into the transformer, producing thereby a "virtual ballast" power supply.[1] This mode of operation causes the power supply to approximate a constant current source without associated dissipative losses. Minimal stress is applied to the circuit components and ripple reduction is aided.

In order to produce the required leakage reactance, a magnetic shunt was used in preference to a series gap, so that stray fields would be minimized.

A photograph of the assembled system is shown in Figure V-2. It represents the setup for cooling an SbSI sample below the Curie point (see Chapter I).

V.2. Perkin-Elmer Spectrophotometer

A double beam grating spectrophotometer (Figure V-3) built to our specifications, is now being used to study radiative processes in the 0.667μ to 34μ range. The instrument uses six gratings and three detectors to cover this range. In addition to this instrument's high resolution, wide range, and versatility of operation, we have introduced a new technique of synchronous sampling (described in Section V-4), thus providing a particularly powerful research tool. The spectrophotometer contains both a source and monochrometer of radiation for the study of infrared absorption in GaAs and similar el materials, either by direct transmission or by reflectance with the aid of a reflectance unit. Alternatively, the monochrometer and recording units alone may be used in analyzing the radiation emitted from el diodes by synchronous sampling. The double beam feature also permits differential measurements, with samples in both beams.

V.3. Low Temperature Equipment

A metal optical cryostat and accompanying vacuum system were constructed and are being used in conjunction with the grating spectrophotometer to carry out transmission and electroluminescence studies at temperatures near 77°K and 40°K. The cryostat (Figure V-4) was designed with twin sample chambers to accomodate the double beam feature of the spectrophotometer. This also allows two samples in succession to be studied at

low temperatures, each in single beam operation, without returning to room temperature and pressure to exchange samples.

The outer vacuum wall of the cryostat body is constructed of 18-8 stainless steel, as are two large metal beakers which form the innter vacuum and liquid helium chambers. The twin sample chambers are each situated at the end of the innermost of three concentric cylindrical legs extending down from the cryostat body. Samples are mounted in thermal contact with a half-inch long silver plug at the end of this leg; the leg itself contains either liquid helium (4.2°K) or liquid nitrogen (77°K). The intermediate leg is of copper and is held at about 77°K by the liquid nitrogen which it contacts through the copper-bottomed nitrogen jacket of the cryostat. The outer leg of each assembly is at room temperature. All surfaces of the legs are gold plated for high reflectance, and the legs share a common vacuum with the rest of the cryostat. Electrical connections to the sample chamber are made by a feed-through mounted on the aluminum alloy cryostat baseplate, with teflon-covered leads running down the outside of the intermediate leg to the sample chamber. The sample chamber (shown in Figures V-5 and V-6 with the outer leg removed) is fitted with sapphire or alkali halide windows, and O-ring vacuum seals are used throughout.

A vacuum-jacketed transfer tube was built and is used to pass liquid helium from a storage dewar to the experimental

cryostat, under a few psi helium gas overpressure. A portable vacuum stand (Figure V-7), which contains both a mechanical pump and a diffusion pump, is used to evacuate the experimental chamber. The cryostat pumps down to about 7×10^{-4} mm Hg in about 20 minutes, to 3×10^{-5} mm Hg when liquid nitrogen is added, and to about 5×10^{-7} mm Hg when liquid helium is added. The drop in pressure with decreasing temperature is due to the condensation of gases which otherwise "outgas" from the large internal surface area of the cryostat. In actual operation, the cryostat is continuously pumped, while the transfer tube is pumped down and sealed off at about 10^{-5} mm Hg.

V.4. Sampling Technique for Spectrophotometer

The Perkin-Elmer light chopper-tuned detector system loses sensitivity and hence resolution for low duty cycle radiation. This happens because the available signal amplitude at the tuned detector frequency drops with the duty cycle of this signal. Since it is necessary to operate the el diodes at low duty cycle for many measurements, means were sought to regain detection sensitivity under these operating conditions. Sampling techniques were found to accomplish this. The system of synchronized sampling that we have developed is capable of adding several orders of magnitude to spectrophotometer sensitivity. This technique is particularly useful in analyzing relatively low intensity emission from el diodes.

V.4.1. Chopped Radiation Detection

A basic spectrophotometer system is shown in Figure V-8(a). Radiation is chopped at 13 cps by mechanical chopper, and after passing through the monochrometer, the chopped radiation is detected and converted to an electrical signal. This electrical signal is a 13 cps square wave having a peak-to-peak amplitude proportional to the output of the radiation detector and thereby proportioned to the intensity of the monochromatized radiation. After amplification, the 13 cps ac signal is linearly converted into a dc signal by the synchronous rectifier which is mechanically coupled to the light chopper, with a phase shift compensating that of the ac amplifier. The dc signal from the synchronous rectifier is presented to the Y-axis of the recorder, causing a Y-axis deflection proportioned to the intensity of the monochromatized radiation. The X-axis on the chart is linearly related to the wave number of the monochromatized radiation.

It should be noted that chopping an ac coupled amplification may be used to eliminate the effects of dc drift in the detector and amplifier. Furthermore, noise reduction by means of bandwidth limitation is easily accomplished by adjusting the amplifier response time at the synchronous rectifier, the response time being essentially the ratio of storage capacitor (C_s) to coupling capacitor (C_c), multiplied by the chopping period $T = 1/13$ sec.

Light chopping as described above is not always prac-

tical, however, and may be impossible under any of the following conditions:

(1) Duty cycle limitations of the radiation emitter do not permit continuous operation.

(2) Dispersion from the emitter may produce excessive losses in the distance between the source and the monochrometer when a light chopper intervenes.

(3) Mechanical arrangements for light chopping may introduce excessive ambient light.

Circumvention of these difficulties, while retaining the advantages of ac amplification/synchronous rectification, is possible by a modification which introduces to the input of the ac amplifier a square wave ac signal synchronized with the rectifier and proportioned in amplitude to the intensity of the monochromatized radiation.

One possible modification is illustrated in Figure V-8(b). A pulse generator excites the radiation emitter at whatever duty cycle that can be tolerated and at a pulse repetition rate well above the synchronous frequency. The output from the radiation detector is a train of pulses which are then integrated to cause a change in the dc level of the detector output. The output of the detector is synchronously interrupted enroute to the ac amplifier and the resulting ac signal is amplified and synchronously rectified. Since the dc output of the synchronous rectifier is proportional to the total dc output of the radiation detector, the recorder must

be zero-adjusted to offset the deflection caused by the output from the radiation detector when the radiation emitter is removed or when excitation is removed from the radiation emitter. Unless the zero signal output of the radiation detector is insignificant or extremely stable, the offset it produces could be troublesome. Furthermore, the synchronous switching at the input to the ac amplifier is capable of introducing objectionable levels of synchronous noise, since the signal level is likely to be very low at this point. The only advantage of this modification is its simplicity and the fact that it does permit operation of the light source within its duty cycle limitation.

A similar modification, inserting the synchronous switching into the radiation emitter's excitation, is shown in Figure V-8(c). This modification does not suffer from the disadvantage of a dc offset, but the achievement of accurate reliable switching at 13 cps is a problem. Even if the switching is reliable, the modification introduces another form of extraneous signal. Unless the pulse repetition rate of the radiation emitter's excitation is an even harmonic of the synhronous operating frequency (13 cps), periodic variations will appear in the amplitude of the signal in the ac amplifier. Furthermore, if these are within the bandpass of the synchronous rectifier, they will cause periodic variations in the recorder input signal which may even appear on the record.

V.4.2. Actual System Built

Suffering none of the disadvantages of the modifications, and offering a substantial increase in the signal-to-noise ratio (20 db or more, depending on duty cycle limitations), is the synchronized sampling system which we are now using. Figure V-9 shows a block diagram of the system and Figure V-10, an event-sequence diagram showing the waveforms present at corresponding points in the block diagram. Figure V-11 is a photograph showing the synchronous contacting mechanism (left side of photo), mounted on a heavy metal disc at the opposite end of the shaft on which the mechanical radiation chopper rotates (right side of photo). The rotating contact is a piece of brass shim stock, which rotates with the disc on the chopper shaft, alternately striking two metal screws set 180° apart (on the face of the box at the left of the photo). As a result, positive pulses are produced at A and B of Figure V-10, at a frequency of 13 pps and with a phase separation of 180°. Pulses occur at C after a time T_M ($\sim$ 25 μsec), which is the minimum delay possible in the pulse generator. Pulses from B and from C are attenuated and summed at D with the 0-5000 ohm variable resistor adjusted so that all pulses have equal amplitude. There results a train of pulses occurring at 26 pps with nearly equal spacing. These are used for triggering the oscilloscopes. Excitation of the radiation emitter is by pulses from A only, and the separation in time, t_T, between V and C is adjustable so that the

output pulses at V occur at the same pulse repetition frequency as the pulses at A, 13 pps, so that if these are presented at the monitor scope, which is triggered at 26 pps, the display will be alternately a baseline and a pulse. Similarly, the presentation on the sampling oscilloscope is alternately a baseline and the radiation detector pulse. Manual display scanning then converts this display into a square wave ac signal.

Display scanning is a sampling technique which in effect magnifies the time scale of a waveform to a sufficiently high degree that the waveform can be reproduced on a mechanical X-Y recorder. In the "manual" mode, the X-axis position at which sampling is to be done, is set manually and the output from the display scanner is then proportional to the vertical deflection. As that portion changes, the output does also. Thus, when the manual scan control is adjusted to scan the oscilloscope display, at a position where the vertical deflection is alternating between baseline and the detector output pulse, the output of the display scanner will be a rectangular wave with an amplitude proportional to the amplitude of the pulse displayed on the scope. Furthermore, with the trigger pulse for initiating the manual scan occurring at a repetition frequency which is twice as as great as the repetition frequency of the pulse being scanned, the display scanner's output is a square wave with the same amplitude.

A comparison of the signal-to-noise ratio of the three systems discussed above emphasizes the great advantage of synchronized sampling. For the purpose of making comparisons, we will assume that the noise in the system is only that of the radiation detector, and that it has an average noise power, N. For the first two modifications, the signal-to-noise ratio, S/N, may be described as the ratio of the average signal power during a semi-period to the average noise power during the same period,

$$S/N = aK/N$$

where

a = peak power during pulse

K = duty cycle of diode excitation

N = average noise power

aK = average signal power

For the synchronized sampling modification used by us, the period to be considered for S/N ratio is δ (see the event sequence diagram, Figure V-10. Therefore, S/N may be expressed as

$$S/N = \frac{\delta a}{\delta N} = \frac{a}{N} \quad \text{for synchronized sampling}$$

Comparing the two systems,

$$\frac{S/N \text{ sync. samp.}}{S/N \text{ sync. chop.}} = \frac{1}{K}$$

Comparison might alternatively be made between the Perkin-Elmer response (with and without sampling stretcher) to an el diode excited at 13 pps with duty cycle K:

$$\frac{\text{S/N (with sampler)}}{\text{S/N (without sampler)}} = \frac{1}{\sin K\pi}$$

In many cases, K will be as small as .001, which would permit a 60 db increase in the S/N ratio by using synchronized sampling. We have, in fact, found such a spectacular improvement to take place. We were generally able to obtain a clean emission spectrum in cases where without synchronized sampling, it was not possible to separate the relatively weak emission line from background fluctuations. As an example, Figure V-11 shows some data on the low temperature ($\sim$100°K) behavior of GaAs electroluminescence. This data was obtained when the synchronized sampling technique was still in the developmental stage, and with the prism spectrophotometer. The data has not been smoothed, and even though much more noise was present at this time than is present in the sampling modification now in the sampling modification now in use, several features of the emission spectrum are clear. The peak has shifted to 1.44 eV and narrowed to 160Å (0.027 eV), as compared with the 1.37 eV position and $\sim$565Å (0.086 eV) width seen at room temperature with the same setup. Some evidence of structure is also present at 1.46 and 1.47 eV, along with the usual long wavelength tail. The $\sim$565Å room temperature width seen with this pre-

liminary sampling apparatus is consistent with the 250Å (.040 eV) separation and 230Å (0.035 eV) and 300Å (0.045 eV) widths for the two peaks, as described above.

Synchronized sampling, in addition to providing an improved S/N ratio, makes it possible to measure accurately the radiation spectrum present at any selected portion of a radiation spectrum present at any selected portion of a radiation emitter's response to step or impulse excitation. In other areas of measurement, the scheme is generally applicable wherever it is desirable to measure an effect caused by a repetitive, time-varying function as a function of some other variable, and at a specific point in relative time (e.g., temperature coefficient of a decay transient).

A photograph of the complete setup using the synchronized sampling technique for spectrophotometry is shown in Figure V-12. The detail showing the light chopper and its switching mechanism is seen in Figure V-13.

REFERENCES (Chapter V)

1. S. Krakauer, "Elimination of the Ballast Resistor in DC Power Supplies", Trans. AIEE, May, 1957.

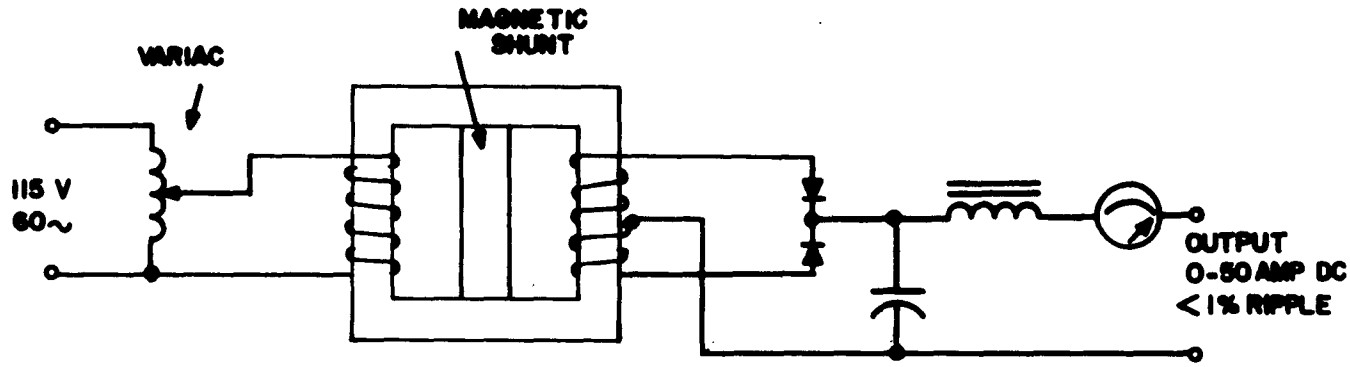

Figure V-1. Thermoelectric Power Supply Circuit Diagram.

Figure V-2. Photograph of Thermoelectric Power Supply Together With Sample of SbSI Mounted in Thermocouple.

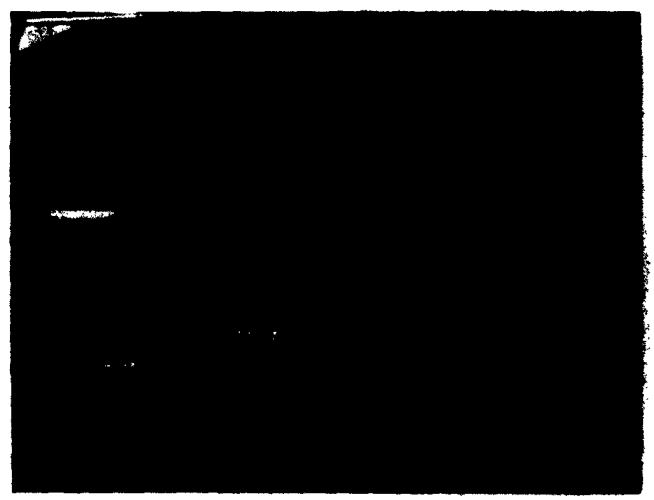

Figure V-3. Photograph of the Perkin-Elmer Double Beam Grating Spectrophotometer.

Figure V-4. Photograph of Metal Optical Cryostat.

Figure V-5. Photograph of the Cryostat Sample Chamber.

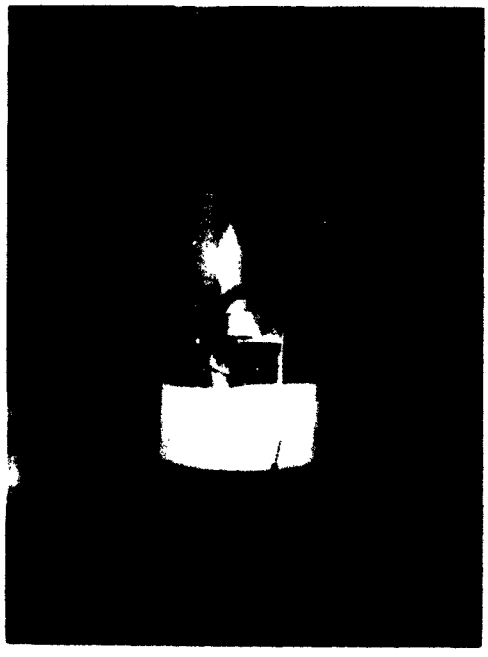

Figure V-6. Photograph of Same as Figure V-5, Except the the Outer Leg Removed.

Figure V-7. Photograph of the Portable Vacuum Stand Containing Vacuum Pumps.

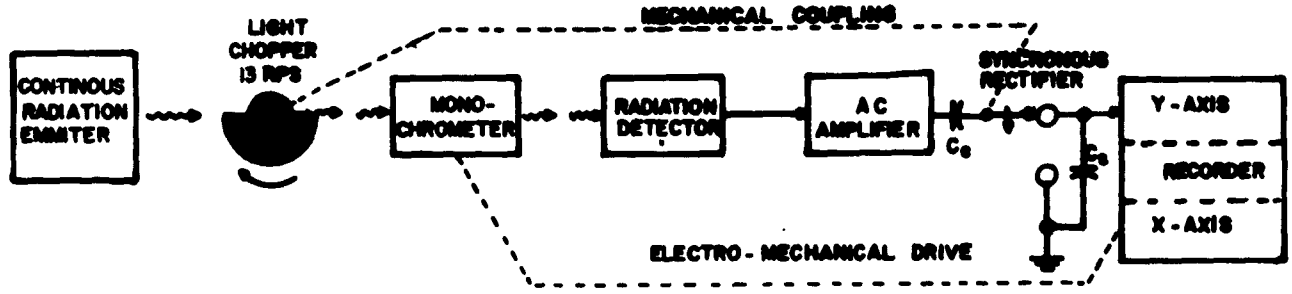

FIG. V-8(a) BASIC SYSTEM OF THE PERKIN-ELMER MODEL SPECTROMETER

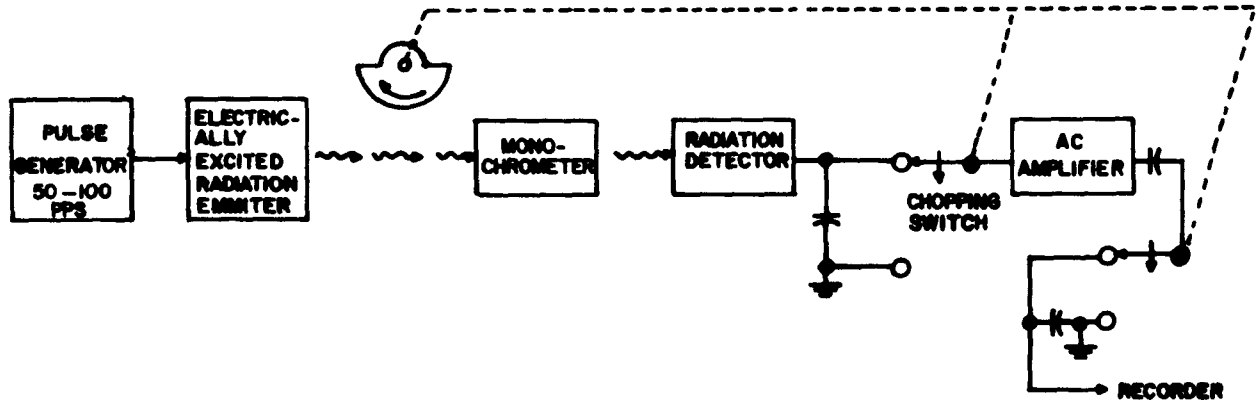

FIG. V-8(b) MODIFICATION WITH SYNCRONOUS SWITCHING OF DETECTOR OUTPUT

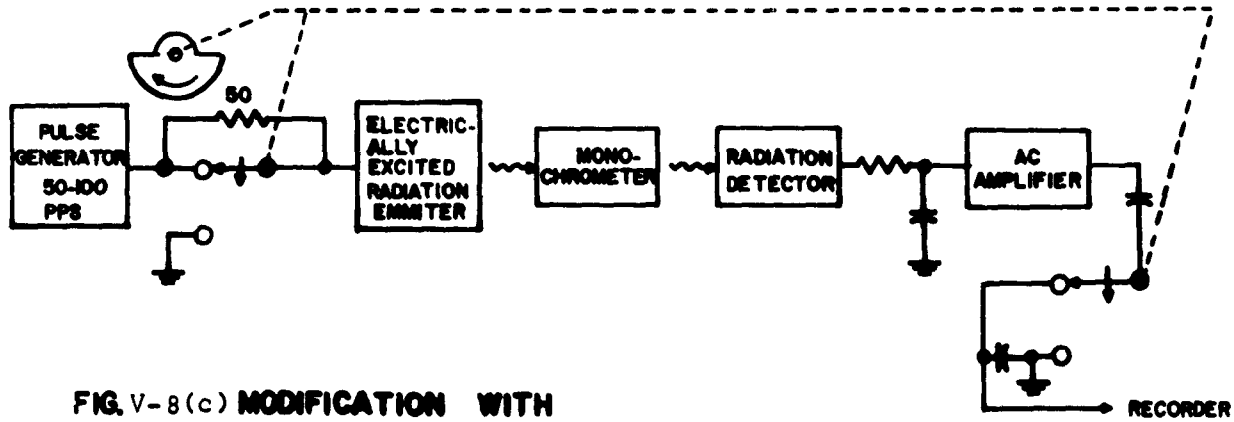

FIG. V-8(c) MODIFICATION WITH SYNCRONOUS SWITCHING OF LIGHT SOURCE EXCITATION

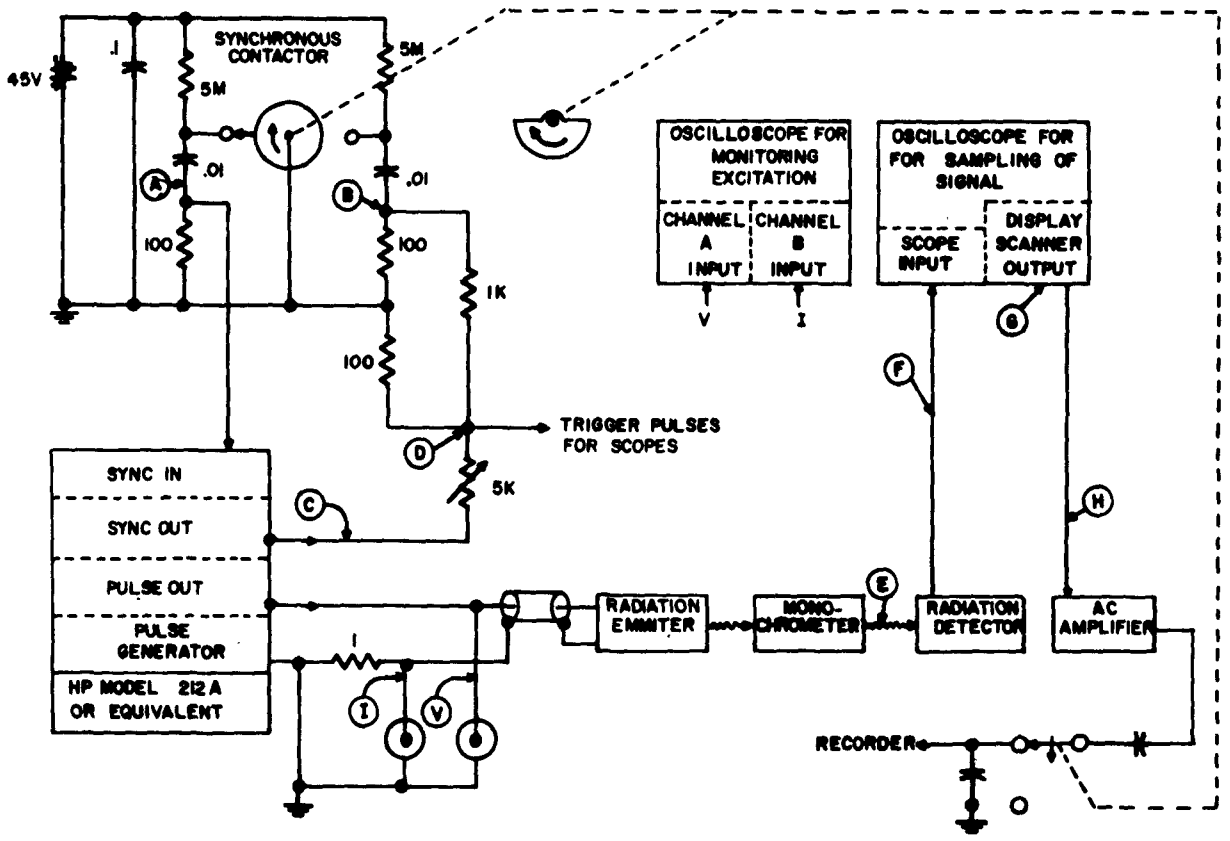

FIG. V-9 BLOCK DIAGRAM OF THE SYNCRONIZED SAMPLING SYSTEM

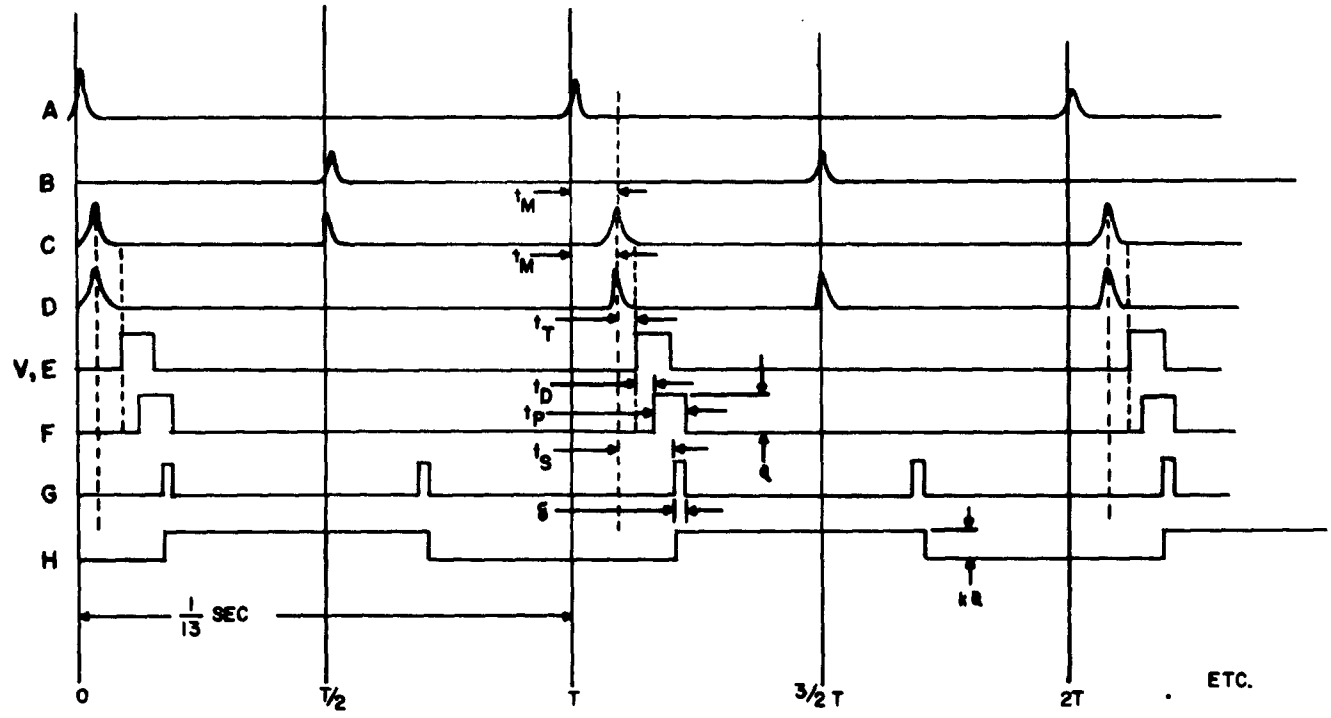

FIG. V-10 EVENT SEQUENCE DIAGRAM OF SYNCRONIZED SAMPLING SYSTEM

KEY: A,B,C,D, etc. are waveforms appearing at the correspondingly identified points in the diagram of Figure V-9.

t_m = minimum time between input pulse and output from pulse generator.

t_T = time-difference between pulse generator's output pulse and output sync (may be adjustable from -10 to +100 microseconds).

t_D = radiation detector's delay in responding to input (typically .025 μsec. for a photomultiplier).

t_S = sampling-scope delay (time between insertion of sync. pulse and the opening of the sampling gate).

δ = sampling time (length of time the sampling gate is open).

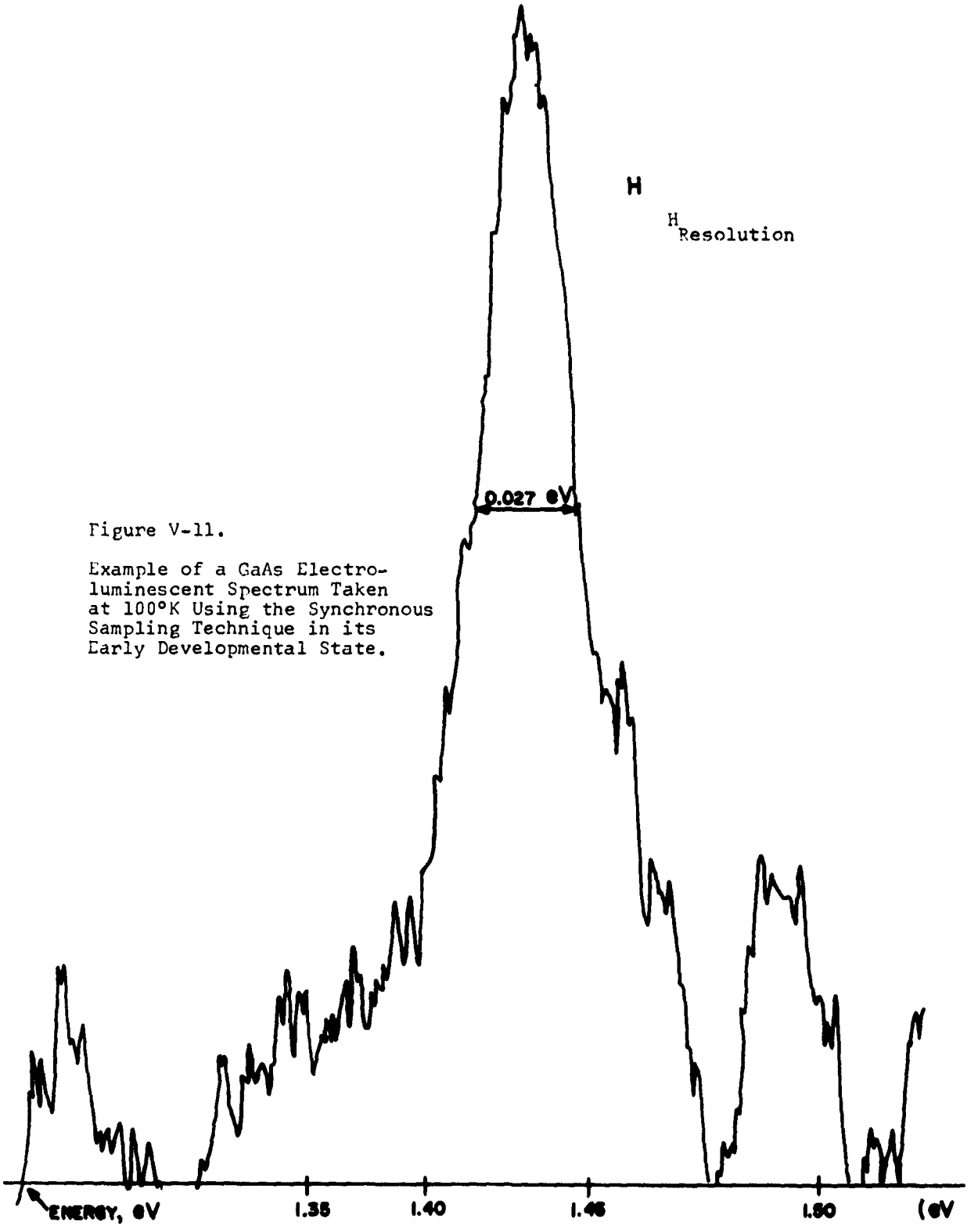

Figure V-11.

Example of a GaAs Electro-luminescent Spectrum Taken at 100°K Using the Synchronous Sampling Technique in its Early Developmental State.

Figure V-12. Photograph of the Synchronized Sampling Setup.

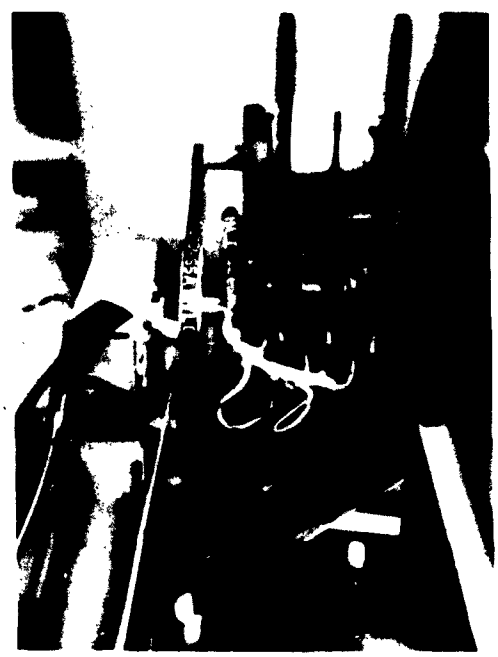

Figure V-13. Photograph of the Detail Showing the Contacting Mechanism Mounted on the Chopper.

CHAPTER VI

MATERIALS SYNTHESIS AND CRYSTAL GROWTH

The effort of the materials synthesis and crystal growth group during this report period has been on: (1) the growth of materials in which radiative recombination processes of injected carriers has been observed, e.g., epitaxial GaAs and single crystal BP; and (2) the synthesis or application of various materials necessary to the study of device physics and/or technology, e.g., thin film CdS and high refractive index glasses.

VI.1. Gallium Arsenide Epitaxial Growth by Vapor Transport

VI.1.1. Introduction

In the previous report, the method for preparing gallium arsenide epitaxial layers in a horizontal gradient furnace was described. Several problems were encountered. One problem, in particular, was the corrosion of the copper tubing and brass fittings in the hydrogen line by back diffusion of hydrogen chloride. The corrosion products were transported into the apparatus contaminating the gallium arsenide epitaxial layers. This led to the erroneous speculation that varying the arsenic pressure gave p-type layers by introducing excess arsenic into the crystal lattice. While waiting for the stainless steel fittings and tubing, some gallium arsenide epitaxial experiments were conducted in an apparatus designed for vertical flow

of the transporting gases and RF heating of the source and substrate. The results were quite successful. Further work with the gradient furnace and its problems was discontinued. The new apparatus and results are described below.

VI.1.2. Experimental

The apparatus used in this investigation is shown schematically in Figure VI-1. Basically, it consists of a vertical reaction chamber, a source of pure hydrogen, iodine, arsenic, a source of gallium arsenide, a single crystalline substrate, and RF heater. The outer reaction tube was constructed from quartz. The inlet for the gases to the reaction tube at the top was extended and formed into a bell-shaped dome. The bottom edge of the dome was ground flat to provide good physical contact between the gas inlet and the graphite pedestal. The intimate contact between the two parts was required to confine the gas flow over the gallium arsenide source and the substrate with a minimum of gas flow around the outside of the graphite.

The graphite pedestal was especially contructed to provide the necessary temperatures to serve as source crucible and substrate holder, and to serve as reaction chamber and transport tube for the gallium and arsenic compounds during growth of the epitaxial layers. The pedestal is shown in Figure VI-2 with the various parts displayed. The round piece with many small holes was installed in the center hole of the upper part of the

pedestal to serve as the bottom of the crucible for the gallium arsenide source. The substrate was placed on the square flat piece which is located in one of the shelf positions in the lower part of the pedestal. The fourth piece shown is part of the support for the pedestal when installed in the reaction tube.

Polycrystalline gallium arsenide was crushed into rather coarse particles and screened to remove the fine pieces which would pass through the holes in the bottom of the crucible. About 25 grams of source material was used. The gallium arsenide substrate, mechanically and chemically polished, was placed on the shelf in the top position so that the substrate was between 0.125 and 0.5 inch from the GaAs source.

After the apparatus was assembled, as shown in Figure VI-3, and purged first with dry nitrogen followed by pure hydrogen, the arsenic was heated to 175°C to 225°C in a stream of hydrogen flowing at 300-500 cc/min. With the RF coil positioned such that the maximum temperature was located at the top of the gallium arsenide source, the crucible was heated to 950°C with the hydrogen containing arsenic vapor passing through the apparatus. Heat conduction from the hot part of the crucible provided 800-850°C for the substrate. After the operating temperature was reached, hydrogen was passed over iodine cooled by an ice bath to 0°C at a flow rate of 200-800 cc/min. The resulting gaseous mixture, hydrogen, arsenic, and iodine, passing

over the gallium arsenide source, transported GaAs source material to the substrate.

VI.1.3. Results

After a few preliminary runs to find the best locations for the heating coil, epitaxial layers were deposited onto a chemically polished GaAs substrate, 111 B. The surface of the layer is shown in Figure VI-4. In many experiments to improve the surface condition, the influence of iodine concentration, temperature, flow rate, and arsenic concentrations were studied.

When the iodine concentration was too high, for example, iodine source temperature 20°C, flow rate 800 cc/min., etching of the substrate was usually observed. This was no problem for a wide range of flow rates (150-500 cc/min.) if the iodine source was cooled to 0°C.

A wide variation of results was obtained with each change of position of the RF load coil with respect to the GaAs source and substrate. When the hottest zone was too high above the source, GaAs was transported from the top pieces to the bottom pieces of the source. When the hottest zone surrounded the lower part of the source material, the substrate was generally etched. These problems were minimized by positioning the RF coil at the top of the GaAs source which established a temperature gradient over the source and substrate.

Several epitaxial slices were prepared using substrate slices ⟨111⟩ B orientation, mechanically and chemically polished. The RF coil was positioned at the top of the GaAs source which gave 950°C at the source and 850°C for the temperature of the substrate as determined by an optical pyrometer. A hydrogen flow of 150 cc/min. over iodine at 0°C and of 300 cc/min. over arsenic at 215°C were used. The results are summarized in Table VI-1.

TABLE VI-1

GALLIUM ARSENIDE EPITAXY

Run	Thickness of layer, Microns	Resistivity of layer, ohm-centimeter	Weight Loss of source, mg	Surface Properties of Layer
A	4.5	0.14	50	bright, smooth
B	4.3	0.12	35	bright, some growth pyramids
C	4.4	0.13	47	bright, smooth

The microphotograph shown in Figure VI-5 is representative of the surfaces obtained. The layer thickness was determined by standard lapping and staining techniques using n-type layers grown on p-type substrates (Cd doped) and was found to be uniform over the substrate with areas of 100 square mm. The source material was 0.17 ohm-centimeter n-type which gave the resistivities indicated in the above Table. The resistivity was determined by the standard four-point probe.

The procedure has been used to prepare 8 micron thick n-type epitaxial layers on heavily doped n-type substrates. The resitivity of the epitaxial layer was determined from capacitance-voltage data obtained from evaporated gold dot diodes prepared on the surface of the layer. The resistivity was in agreement with the above four-point probe data. The epitaxial slices are being used in some device investigations which are, as yet, incomplete.

VI.1.4. Conclusions

An apparatus using a vertical flow of gases and vapors to transport gallium arsenide has been demonstrated. This arrangement improves the efficiency of the transport process providing shorter growing times and decreases the period for diffusion of impurities or dopants from the substrates into the epitaxial layer. In addition, the thickness of the layer is very uniform over the surface of substrate slices which have large surface areas, i.e., greater than 1 cm^2. With the more convenient arrangement, more experiments can be conducted with a great variation in temperature and temperature gradient.

VI.2. Thin Film CdS-GaAs Heterojunctions

Semiconductor grade cadmium sulfide-indium sulfide (sesqui) mixed powders (0.1-0.8μ particles) have been evaporated in vacuum equipment, as shown in Figure VI-6, forming films on various substrates; in particular, p-type GaAs, 0.2 ohm-cm and also quartz flats for optical evaluations.

The CdS:In layers have been deposited onto the heated GaAs substrates in the form of circular dots, 8μ thick and 300μ in diameter, with bulk resistivity 2×10^{-3} ohm-cm. Ohmic contacts were made to the degenerate CdS by means of evaporated In dots registered with respect to the CdS, as shown in Figure VI-7.

Preliminary electrical measurements of these heterojunctions indicate a saturation current, I_s, of $\approx 10^{-8}$ amp and a forward resistance of 30 ohms at 1.5×10^{-2}. Inasmuch as both values appear to be too high for efficient injection luminescence, further work is planned to elucidate the source of the series resistance, as well as the leakage resistance in these diodes. It is expected that improvements in heterojunction quality will follow experimentation carried out in a liquid nitrogen trapped, lower ultimate pressure vacuum system. A more detailed discussion of these heterojunctions is presented in Chapter III.

VI.3. Solution Growth of Boron Phosphide

As a means of increasing the crystallite size and purity of boron phosphide, the synthesis and growth of boron phosphides from melts of $Ni\text{-}P_{(excess)}$ and $Ni\text{-}B_{(excess)}$ has been investigated. The experiments to date have been largely exploratory with the primary emphasis placed on the determination of the most critical process parameters.

VI.3.1. Experimental

The apparatus used in this investigation is shown schematically in Figure VI-8 and pictorially in Figure VI-9. It consisted of a hood-enclosed horizontal tube furnace with Sillimanite reaction tube, a source of purified argon, and the necessary stepless-proportional temperature controllers.

The materials used in this work were:

(1) Argon, purified by treatment with CaH_2 at 400°C followed by Zr treatment at 900°C.

(2) Red Phosphorus, 99.999+%, United Mineral Company.

(3) Nickel Sponge, 99.999+%, Johnson, Matthey & Co.

(4) Boron Powder, 99.999%, Mackay Company.

The synthesis procedure consisted of three separate processes:

(1) The preparation of Ni-P and/or Ni-B alloys by reaction of the elements in evacuated quartz tubes.

(2) Reaction and dissolution of either the Ni-P alloys with boron at 1300 to 1500°C or the Ni-B alloys with $P_{4(g)}$ at 1300 to 1500°C.

(3) The slow cool-down of the solution and, hence, the nucleation and growth of boron phosphides followed by HNO_3-HCl etching to remove excess Ni, Ni-B and/or Ni-P.

It was established by means of wet analyses that when excess phosphorous was used in the Ni melt growth, the formation of f.c.c. BP of nearly stoichiometric composition, B/P ratio $\approx$1.1, could be obtained, whereas, if excess boron was used, the composition of the BP obtained was highly variable with B/P ratios of 7.3 to 1.5. The crystal structure was complex and the crystals had a blue to brown color (See Figures VI-10 and VI-11). It is important to note that in all cases, the boron phosphides produced were always p-type with resistivities from 0.4 to 0.09 ohm-cm and would produce electroluminexcence upon probing with a tungsten contact and the passage of >20 ma current.

The necessary growth conditions have been established for the reproducible production of f.c.c. BP crystals (See Figures VI-12 and VI-13) with yields of greater than 30% basis boron; however, all of the boron phosphides produced to date by the Ni melt method have contained large amounts of Ni and/or NiP inclusions which tended to strain the crystals. The solution of these problems will be attempted by a programmed cooling cycle at cooling rates below 0.1°C per minute, thereby slowing down growth rate.

N-type, f.c.c. BP, 0.03 ohm-cm crystals have also been grown in the same manner as the p-type material except for the incorporation of sulfur at a concentration of 800 ppm in the total Ni-P-B melt.

VI.4. High Refractive Index Glasses

The syntheses and physical property determinations of low melting glasses which could provide suitable optical coupling within GaAs-Si Functional Electronic Blocks have been carried out.

(1) $n_{8500 \text{ to } 9500\text{Å}} = 3.5$.[1]
(2) Low optical absorption in the region 8500-9500Å.
(3) Resistivity greater than 10^{10} ohm-cm @ 60°C.
(4) Melting point below 300°C.
(5) Minimum dielectric constant @ 1 mc.
(6) Devitrification should be minimal.

To these ends, three groups of glasses were prepared and their properties measured:

(1) As-S glasses[2,3] within the glass forming region, 18 to 65% wt. As.
(2) As-S-Se glasses.[4]
(3) As_2S_3-Sb_2S_3 glasses.[5]

VI.4.1. Experimental

All of the glasses were prepared by direct reaction of the elements in an evacuated, quartz ampoule at 500°C for 24 hours. The sulfur, selenium and antimony were 99.999+% purity, ASARCO, while the arsenic was reagent grade Baker & Adamson, further cleaned by etching with conc. HCl and washing-drying with anhydrous methanol.

The indices of refraction were measured visually and only approximately microscopically and the spectral transmission were measured with a Beckman DK-1 spectrophotometer. A summary of composition and physical properties of these glasses is shown in Table VI-2, with optical transmission curves in Figures VI-14, VI-15, and VI-16.

VI.4.2. Conclusions

While the As-S glasses had the best optical properties beyond the absorption edge, the highest refractive index was 2.7. Improvement in properties was obtained by incorporation of selenium in As-S glasses; however, the highest refractive indices were obtained in the As-Sb-S system and appear to be the most promising for further development and measurement.

TABLE VI-2

PHYSICAL PROPERTIES OF SOME GROUP V-VI GLASSES

Sample Number	Molecular Composition	Index of Refraction (Approx.)	Melting Point °C	Absorption Edge* Millimicrons
3	$As_2S_{23.0}$	2.0	118	518
4	$As_2S_{10.9}$	2.2	121	520
5	$As_2S_{7.8}$	2.2	165	525
8	$As_2S_{3.5}$	2.37, n_D = 2.39	189	610
7	$As_2S_{3.0}$	2.7	207	590
6.	$As_2S_{2.5}$	non-vitreous	-	-
9	As_2S_3 - 1%Se	2.5, n_D = 2.67	230	612
14	As_2S_3 - 2.5% Se	2.4	231	615
10	As_2S_3 - 5% Se	2.7, n_D = 2.5	218	620
13	As_2S_3 - 10% Se	2.6	210	630
11	As_2S_3 - 25% Se	2.5	206	662
12	$As_2S_{16.6}$ - 18% Se	2.3	142	580
15	As_2S_3-Sb_2S_3 1:3	non-vitreous	-	-
16	As_2S_3-Sb_2S_3 1:1	3.1	246	665
17	As_2S_3-Sb_2S_3 2:1	2.3	229	635

*Taken from inflection point on spectral transmission curves.

REFERENCES (Chapter VI)

1. T. S. Moss, "Optical Properties of Semiconductors", Butterworths Scientific Publications (1959).
2. A. G. Fisher and A. S. Mason, RCA Scientific Report No. 3, Contract No. AF19(604)-8018, November 15, 1961.
3. S. S. Flaschen, A. D. Pearson and W. R. Northover, J. Appl. Phys. 31, 219 (1960).
4. R. Fredericks, J. Opt. Soc. of Amer. 43, 12, p. 1153, (1953).
5. B. T. Kolomiets and B. V. Pavlov, Soviet Physics Solid State, 2, July-December, 1960.

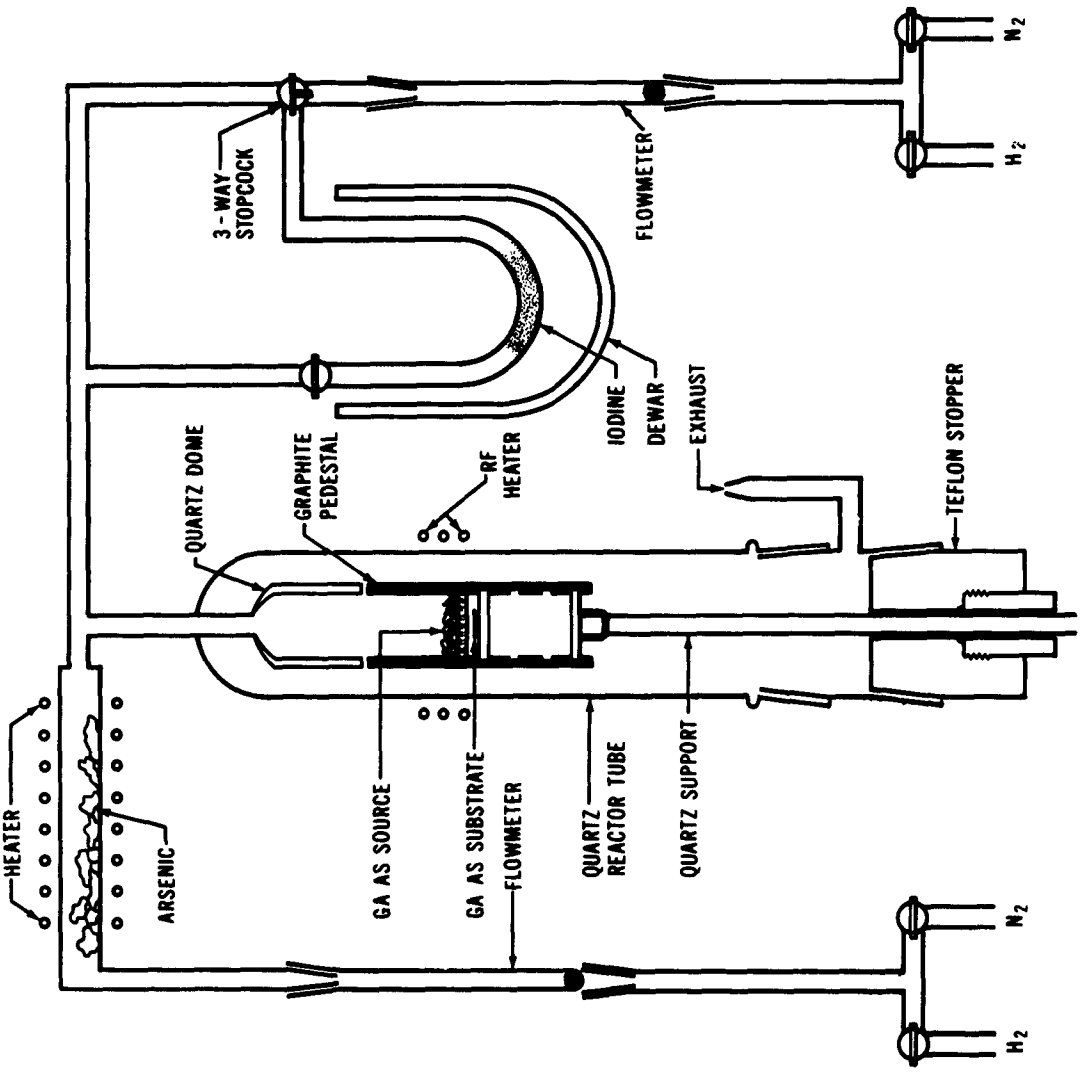

Figure VI-1. Schematic Drawing of GaAs Apparatus

Figure VI-2. Photograph of Graphite Pedestal.

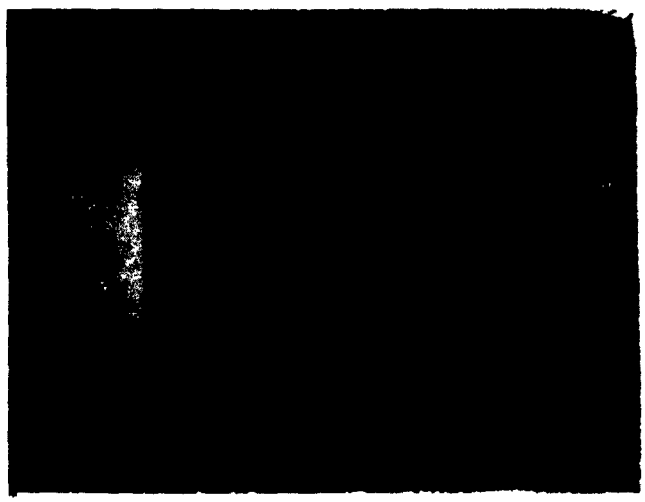

Figure VI-3. Photograph of Assembled Apparatus.

Figure VI-4. Microphotograph of GaAs Epitaxial Layer.

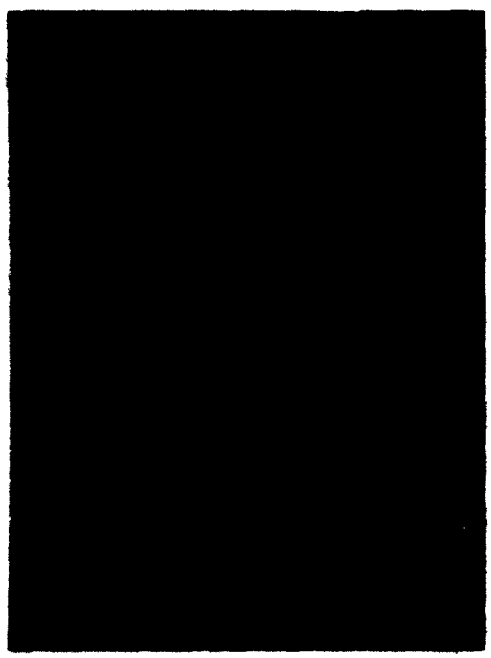

Figure VI-5. Microphotograph of GaAs Epitaxial Layer Prepared Under Optimum Conditions; Pits Due to Dislocations Propagated Through Epitaxial Film Originating in Substrate Material.

Figure VI-6. Vacuum Evaporator Equipped for CdS Evaporation.

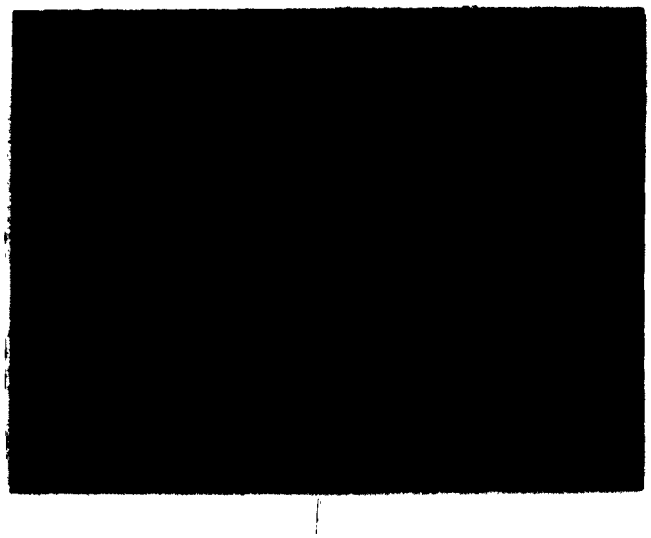

Figure VI-7. Preliminary Heterojunctions of CdS:In-GaAs(p).

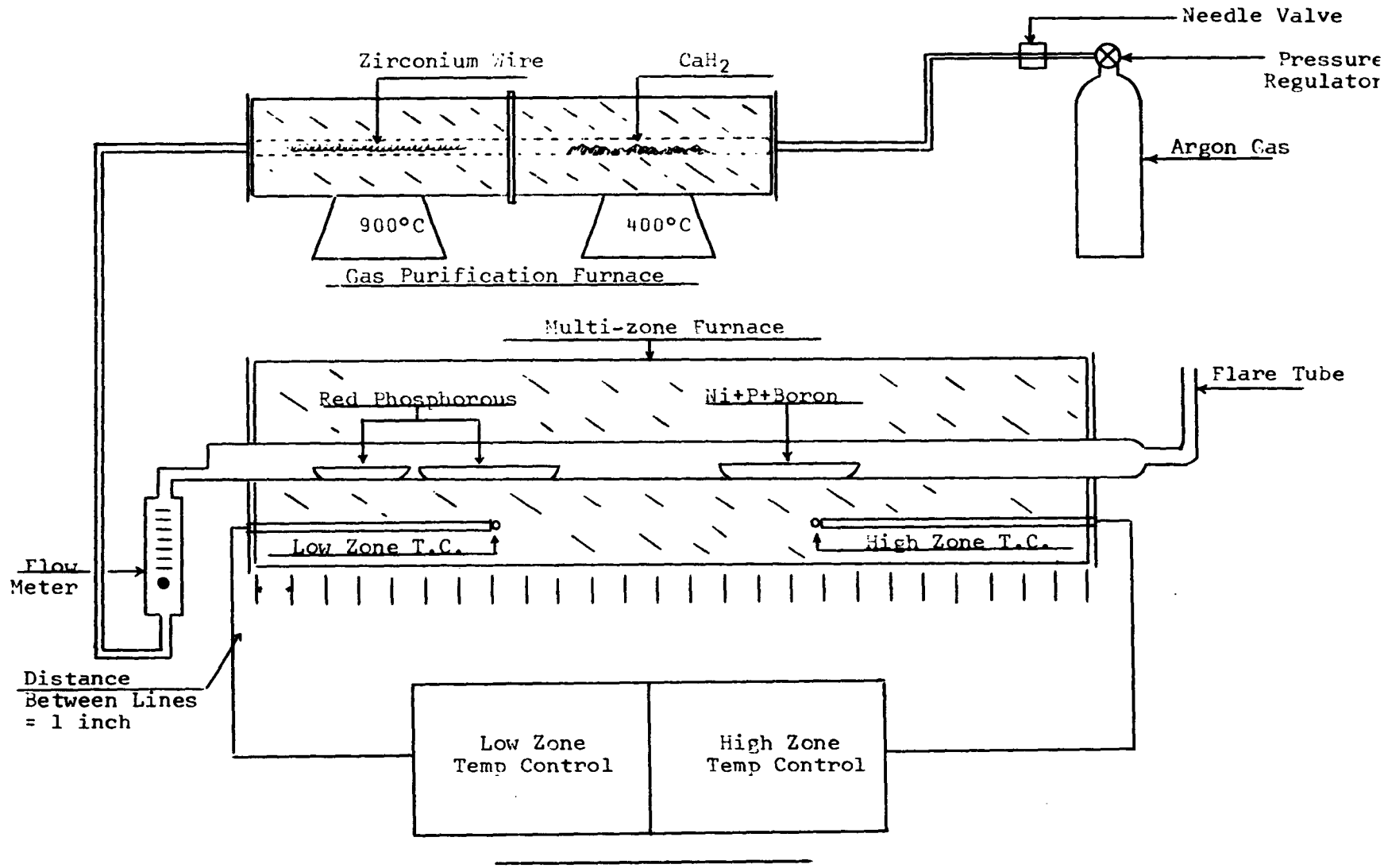

Figure VI-8. Schematic of BP Solution Growth Equipment.

Figure VI-9. High Temperature Furnace and Associated Equipment Used in Growth Experiments.

Figure VI-10. Nearly Perfect Crystal of $B_{13}P_2$.

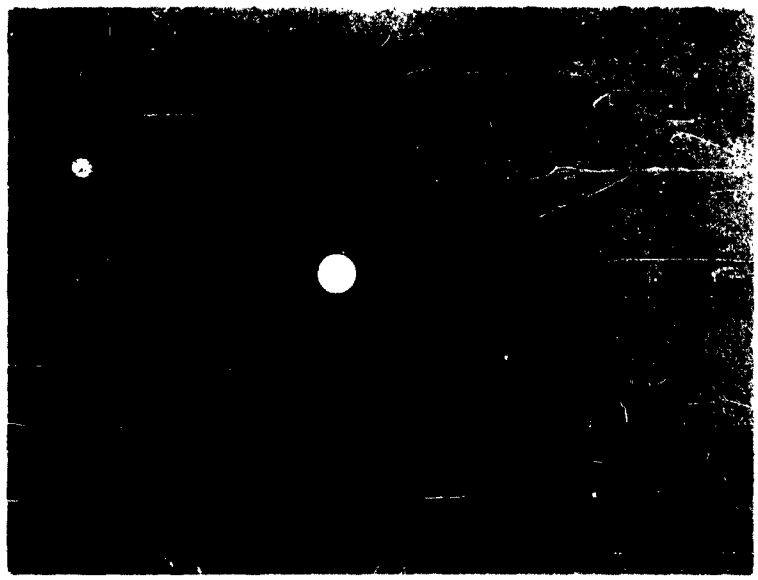

Figure VI-11. X-Ray Back Reflection $\perp$ to Basal Plane of Crystal in Figure VI-10.

Figure VI-12. Face Centered Cubic Crystal of BP, Red-Orange, Plate Plane is || with <111> Plane.

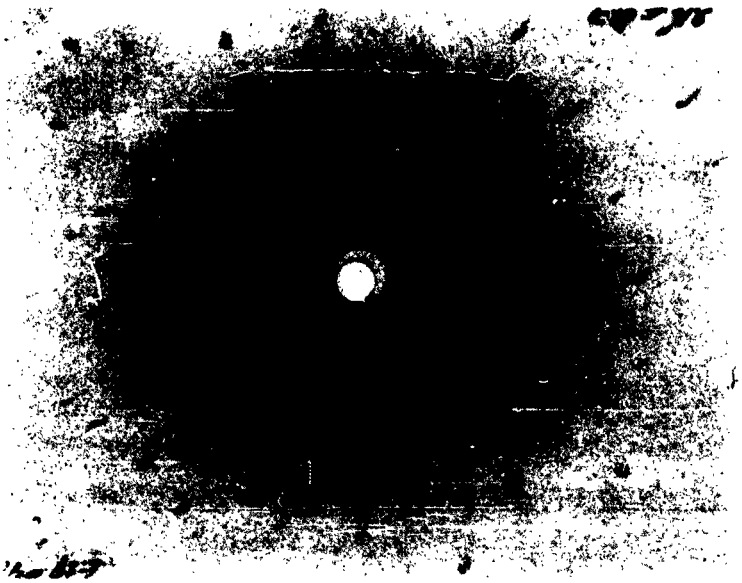

Figure VI-13. X-Ray Back Reflection $\perp$ to Plate Plane of Crystal in Figure VI-12.

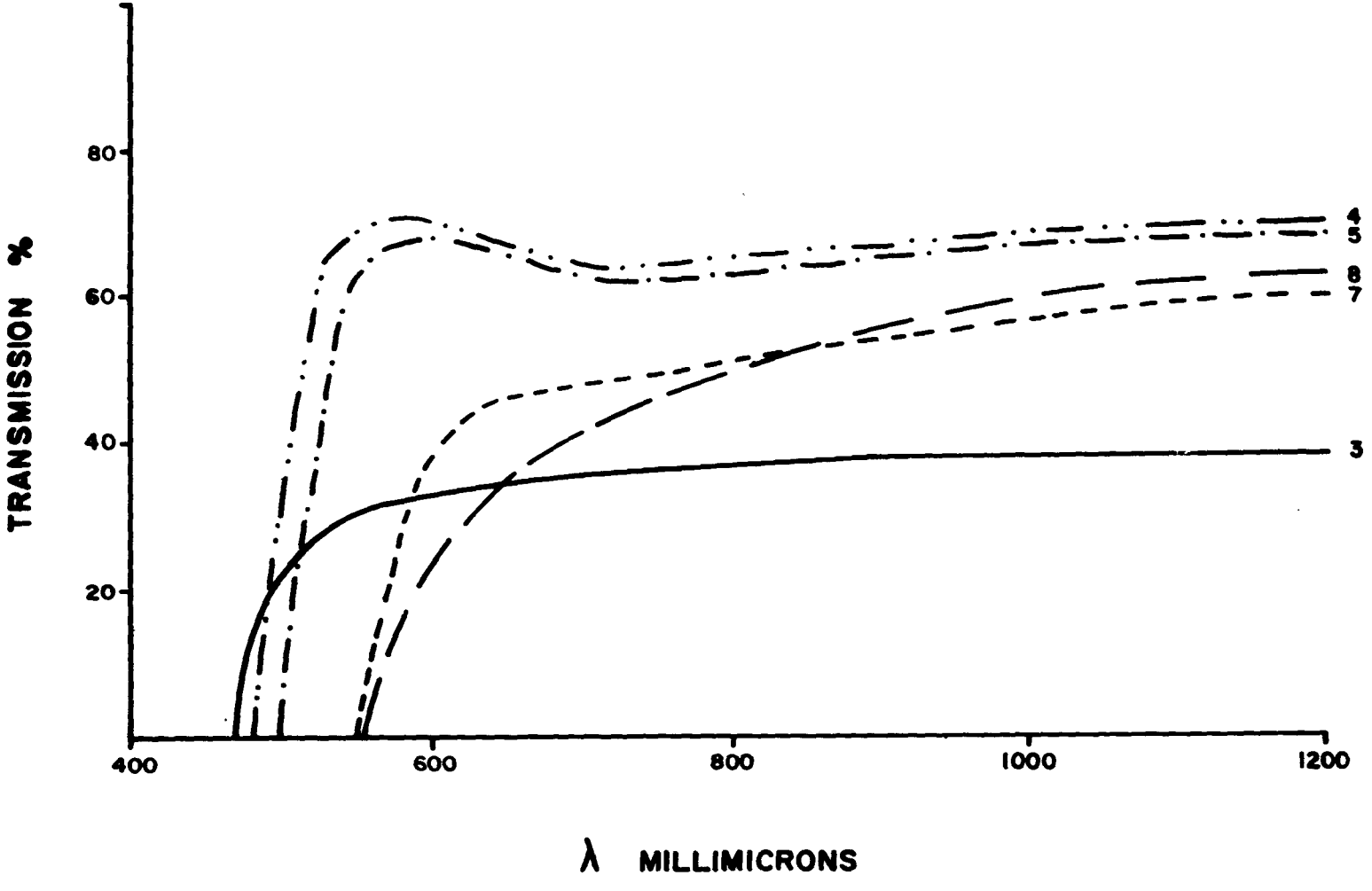

Figure VI-14. Optical Transmission of As-S Glasses, Thickness = 5×10^{3} in.

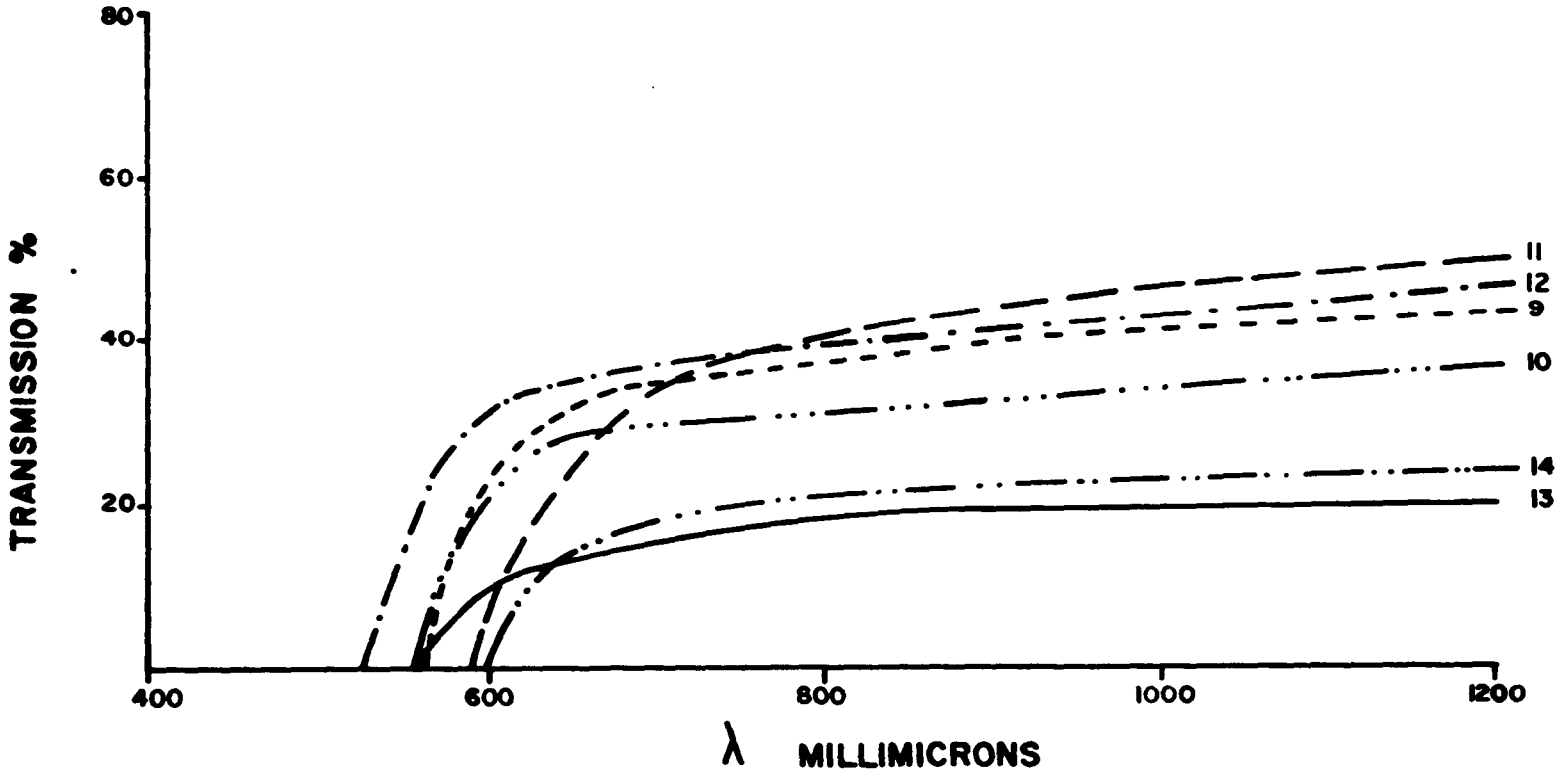

Figure VI-15. Optical Transmission of As-S-Se Classes, Thickness = 5×10^{-3} in.

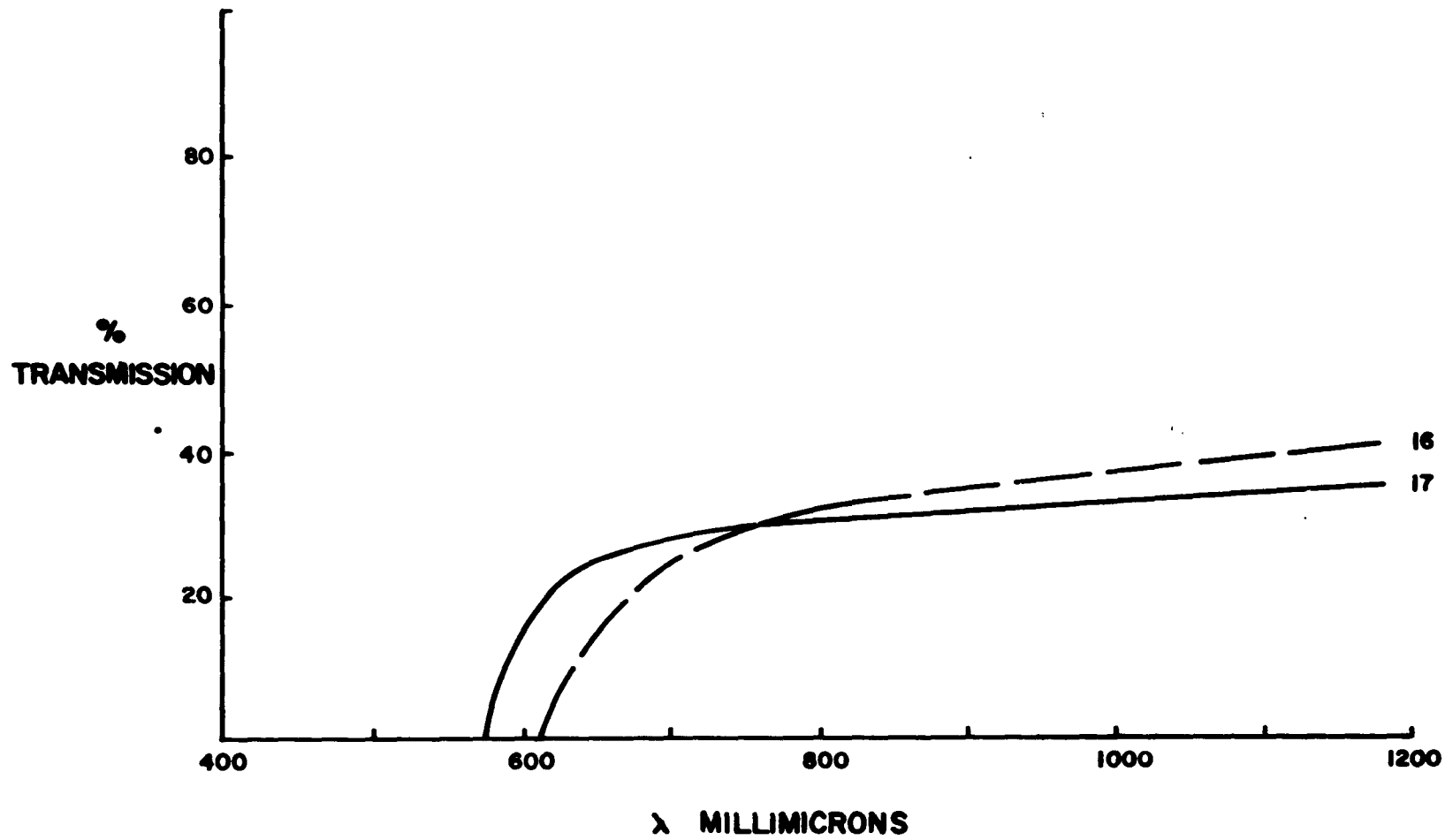

Figure VI-16. Optical Transmission of As-Sb-S Classes, Thickness = 5×10^{-3} in.

CHAPTER VII

SUMMARY

The work falls into three general areas of activity: (1) exploration of solid state effects; (2) experimentation and development of various photosensors and electroluminescent radiators; and (3) experimental design and fabrication of functional electronic blocks. The report has been grouped into six chapters.

In Chapter I, the continued exploration of optical, structural and ferroelectric properties of SbSI is described. Smearing of the optical absorption edge, poor definition of Laue back-reflection x-ray spots, at a low spontaneous polarization and a high coercive field all indicate a poorer crystallinity of our crystals than those reported in the literature. An upper bound of 5% has been tentatively assigned to the photoconductive and ferroelectric coupling in SbSI. A comparison of reported values of the shift of optical absorption edge with electric field in several materials brought out that this effect is at least an order of magnitude larger in SbSI than in any other material.

In Chapter II, the continued effort on photosensors is described. Two distinct families of npn planar silicon phototransistors have been developed. One with gain β of 80-120 and the other of 600-800. The photoelectric collection efficiency is highly uniform over the exposed base and is

approximately 50%. The speed of response of the phototransistors is a function of light intensity, collector capacitance and gain, and emitter capacitance. A representative operational number is about 3 microseconds at 100 ma for the large collector areas used.

A survey of significant parameters of various photoconductor materials potentially useful in optoelectronic networks has been initiated. So far the most encouraging results have been obtained with commercial lead sulfide photoconductors.

Chapter III deals with experimentation on injection electroluminescence and is further subdivided into sections on zinc diffused GaAs pn junctions, n on p GaAs alloyed junctions, GaAs-CdS pn heterojunctions and BP luminescence.

Two studies have been carried out on zinc diffused GaAs junctions. The first deals with effect of Cu on electroluminescence in GaAs. The second concerns fine structure in "Edge Electroluminescence" spectra.

The first study represents the completion of the work dealing with the effect of copper doping in GaAs on the electroluminescence spectrum and on the edge emission.

The second study was carried out using a new synchronous sampling technique. It enabled the resolution of two peaks in the edge luminescence spectrum of GaAs. The old is 1.37 eV and the new at 1.41 eV. The possible mechanisms giving use to the second peak are discussed.

The work on electroluminesenee from diodes made by alloying AgTe dots onto p-type GaAs continued. The most

efficient diodes were made on GaAs with hole concentrations about $2x10^{17}$ acceptors/cm^3.

Heterojunctions of n-type CdS on p-type GaAs have been fabricated. The energy discontinuity of the conduction band edges at the junction has been determined to be 0.2 eV. The saturation current has been found to be far in excess of that expected.

The effects of doping on the far infrared absorption in GaAs have been investigated. It was found that above defect concentrations of $10^{17}/cm^3$ the restrahlen bands were wiped out. The data has been alalyzed to suggest the destruction of the photon-optical phonon transition because of lattice coherence effects. Implications of this on the optical absorption and emission near the band edge in GaAs are discussed.

The electroluminescent spectrum of rhombohedral boron phosphide has been obtained.

In Chapter IV on Optoelectronic pairs, preliminary experiments leading to the development of an optimum optical match between the el diodes and photosensors are described.

In Chapter V various instrumentation built or installed during the last period in support of the program is described. These include a power supply for the thermoelectric cooler, the installation of a new double beam grating spectrophotometer construction and installation of an optical cryostat of novel design and the development of a new synchronous sampling technique for the spectrophotometer.

In Chapter VI all of the materials synthesis and crystal growth effort is described. It includes gallium arsenide epitaxial growth by vapor transport, boron phosphide growth from solution, evaporation of CdS thin films onto GaAs substrates and the synthesis of high refractive index glasses.

CHAPTER VIII
CONCLUSIONS

1. Optical, ferroelectric and structural measurements of our SbSI crystals indicate that they are less perfect than those previously grown by others.
2. The photoferroelectric effect in SbSI appears to be a second order effect (at least in our crystals).
3. The shift of the optical absorption edge with electric field in SbSI is at least an order of magnitude larger than in any other investigated solid state material.
4. Silicon phototransistors having gains β as high as 800 have been constructed.
5. The speed of response of the developed Si phototransistors is size and material limited.
6. Lead sulfide photoconductors appear to have the sensitivity needed in optoelectronic networks using GaAs el diodes.
7. The speed of response of PbS photoconductors is significantly inferior to that of Si phototransistors.
8. The 1.0 eV emission band in the electroluminescent spectrum of GaAs diodes is caused by dissolved copper.
9. Copper contamination can significantly decrease the radiant output of the 1.37 eV band and thus the transfer efficiency of GaAs electroluminor-Si photosensor matched pairs.
10. Spectrosil quartz minimizes copper contamination during high temperature treatments of GaAs.
11. A high energy satellite peak located at 1.41 eV has been discovered associated with the main 1.37 eV peak in the

GaAs electroluminescent spectrum at room temperature.

12. The optimum concentration of holes in p-type GaAs used for the fabrication of AgTe alloy diodes is close to $2 \times 10^{17}/cm^3$.

13. Cadmium and zinc doped GaAs gives the same room temperature electroluminous quantum yield in alloy junctions.

14. The electroluminous quantum yields of alloyed and diffused GaAs pn junctions are comparable.

15. In theory, the n-type CdS on p-type GaAs heterojunctions, appear as on ideal el diode structure.

16. Early experiments on CdS-GaAs heterojunctions are analyzed to exhibit an excess current component, which does not consist of injection of electrons into the neutral region of the GaAs.

17. A bleaching of the restrahlen bands in GaAs (0.033-0.039 millielectron volts) with doping in excess of $10^{17}/cm^3$ has been established.

18. A hypothesis of concentration quenching of the k = 0 optical phonons in GaAs is proposed and used to explain the optical absorption anomalies at the band edge requiring a re-interpretation of the energy band picture in undoped GaAs in terms of direct but phonon assisted transitions.

19. A second type of boron phosphide, which has a rhombohedral rather than cubic structure, exhibits electroluminescence in two main bands situated at 2.9 eV and 2.2 eV.

20. Spatial distribution studies of various diffused junction GaAs el devices indicate that the major contribution to

the losses incurred in coupling el diodes to photosensors does not come from self-absorption but from geometrical optics and other geometrical factors.

21. A significant improvement in sensitivity during spectrophotometry of pulsed el devices can be obtained by a synchronous sampling technique.

22. Improvement in efficiency and quality of vapor transport and deposition of GaAs epitaxial layers has been obtained substituting a vertical flow for horizontal flow setup.

23. No conclusions have been reached yet concerning the CdS thin film technology needed for heterojunction fabrication.

24. The necessary growth conditions for reproducible production of cubic boron phosphide have been established.

25. Undoped boron phosphide is p-type.

26. Sulfur doped, n-type cubic boron phosphide has been grown with conductivities as low as 0.003 ohm-cm.

27. High index of refraction glasses have been obtained within the As-Sb-S ternary system.

CHAPTER IX

RECOMMENDATIONS

It is recommended to:

(1) Continue the exploration of electro-optical effects in SbSI, if and after better crystals become available.

(2) Develop higher speed of response Si phototransistors.

(3) Continue to search for suitable photoconductors.

(4) Use spectrosil quartz in the fabrication of all GaAs el devices.

(5) Continue the study of electroluminescent phenomena; to study the temperature effects on the emission and absorption spectra in GaAs in order to solve the problem of identifying the mechanism of efficient light emission.

(6) Continue the study of alloyed GaAs junctions and further optimize their performance.

(7) Continue the fabrication of heterojunction diodes using CdS on GaAs and determine the cause of their excess current.

(8) Extend the study of optical phonons in GaAs to lower and higher temperatures.

(9) Continue the study of electroluminescence in boron phosphide.

(10) Continue the work on optimization of light coupling between matching pairs of electroluminescent and photosensor devices.

(11) Design and construct a chopper optoelectronic network.

(12) Grow improved SbSI crystals.

(13) Improve crystal growth of boron phosphide and investigate the boron rich side of its phase diagram.

(14) Study the details of the CdS thin film growth on GaAs.

(15) Explore vapor transport and epitaxial growth of selectively doped GaAs layers.

(16) Continue the study of high index of refraction glasses.

CHAPTER X

PERSONNEL

The following workers contributed to the effort during this report period:

L.R. Anderson
M.M. Atalla
C.A. Austin
R.H. Bube
O.R. Cook
W.C. Davis
J.T. Diesel
R.G. Drabin
B.D. Eiseman
N. Erickson
R.E. Ewing
P.E. Greene
R.L. Hutton
G.W. Justusson
S.M. Krakauer
T.B. Larsen
B.B. Lewis
E.E. Loebner
D.H. Lowndes
H. Luechinger
K.M. Malone
G.H. Marshall
R.E. Parr
E.G. Pollard
F.A. Rogers
D. Samsonovs
A. Simonini
L.F. Sobon
H.O. Sorensen
N.G. Spilling
R.W. Teichner
A.C. Welch